The Astronomical Journal, 158:246 (25pp), 2019 December https://doi.org/10.3847/1538-3881/ab2df3

Surface Imaging of Proxima b and Other Exoplanets: Albedo Maps, Biosignatures, and Technosignatures

S. V. Berdyugina[1,2] and J. R. Kuhn[2]
[1] Leibniz Institut für Sonnenphysik (KIS), Schöneckstrasse 6, D-79104 Freiburg, Germany; sveta@leibniz-kis.de
[2] Institute for Astronomy/Maui, University of Hawaii, 34 Ohia Ku Street, Pukalani, HI 96768, USA; kuhn@ifa.hawaii.edu
Received 2017 October 30; revised 2019 June 8; accepted 2019 June 27; published 2019 November 25

Abstract

Seeing oceans, continents, quasi-static weather, and other surface features on exoplanets may allow for detecting and characterizing life outside the solar system. The Proxima b exoplanet resides within the stellar habitable zone, possibly allowing for liquid water on its surface, as on Earth. However, even the largest planned telescopes will not be able to resolve its surface features directly. Here we demonstrate an inversion technique to indirectly image exoplanet surfaces using observed unresolved reflected light variations over the course of the exoplanet's orbital and axial rotation: ExoPlanet Surface Imaging (EPSI). We show that the reflected light curve contains enough information to detect both longitudinal and latitudinal structures and to map exoplanet surface features. We demonstrate this using examples of solar system planets and moons, as well as simulated planets with Earth-like life and artificial structures. We also describe how it is possible to infer the planet and orbit geometry from light curves. Then, we show how albedo maps of Proxima b can be successfully reconstructed for tidally locked, resonance, and unlocked axial and orbital rotation. Such albedo maps obtained in different wavelength passbands can provide "photographic" views of distant exoplanets. We estimate the signal-to-noise ratio necessary for successful inversions and analyze telescope and detector requirements necessary for the first surface image reconstructions of Proxima b and other nearby exoplanets using EPSI. This is a significant challenge, but the success of such measurements depends heavily on large-aperture diffraction-limited telescope performance—a feat that may be achieved on the ground before it is in space.

Key words: methods: numerical – planetary systems – planets and satellites: surfaces – scattering – techniques: photometric

1. Introduction

Maps of planetary surfaces provide records of their evolution. Surface alterations through cratering, weathering, geological processes, or various life-form activities (including intentional geoengineering) leave their marks on planetary surfaces. Revealing such records on solar system bodies was a challenge until space missions visited some of them. More than 100 yr ago, Russell (1906), in a seminal paper, described how the surface shape and features of unresolved moons and asteroids, as well as their rotational axes, can be recovered from reflected light-curve photometric time series. Guthnick (1906) applied it to map some of Saturn's satellites. More recently, such light-curve inversions produced surface maps of Saturn's moon Iapetus (Morrison et al. 1975) and Pluto and Charon (see Buie et al. 1997). Main albedo features recovered indirectly on their surfaces were later confirmed by spacecraft measurements. Recovering asteroid shapes and morphology from light-curve inversion (including polarimetry) is also proven to be successful (e.g., Kaasalainen et al. 1992; Carbognani et al. 2012).

Resolving surface features (e.g., continents) or global weather patterns on even the nearest exoplanets through direct imaging requires optical systems many km in size; this will not happen soon. On the other hand, emitted and reflected planet light has been detected from exoplanet host stars by different observing techniques in a few cases. The *Spitzer* space telescope measured the IR light curves of hot Jupiters and detected enhanced emission longitudes ("hot spots") in their atmospheres (e.g., Harrington et al. 2006; Knutson et al. 2007; Cowan & Agol 2008; Crossfield et al. 2010). However, the latitudinal information could not be yielded from these data. High-precision polarimetry has provided first albedo and color measurements for a hot Jupiter (Berdyugina et al. 2008, 2011). Similarly, the *CoRoT*, *Kepler*, and *Hubble* telescopes achieved the sensitivity to detect optical and near-UV reflected light curves from hot Jupiters (e.g., Snellen et al. 2009; Demory et al. 2011; Evans et al. 2013; Faigler & Mazeh 2015).

Model solutions for exoplanet albedo maps and orbital parameters based on reflected flux or polarization light curves have also been demonstrated (e.g., Cowan et al. 2009; Fluri & Berdyugina 2010; Kawahara & Fujii 2011; Fujii & Kawahara 2012; Schwartz et al. 2016; Cowan & Fujii 2017; Cowan et al. 2017). Ford et al. (2001) computed integrated reflected light from an Earth-like exoplanet. Cowan et al. (2013) showed that under some circumstances, orbital and some exoplanet latitudinal information can be derived from the integrated time-dependent exoplanet thermal emission. Secondary eclipse observations can also reveal latitudinal information under certain geometry (Rauscher et al. 2007; de Wit et al. 2012; Majeau et al. 2012).

We consider here the light-curve inversion problem assuming the possibility of high-sensitivity direct imaging of the exoplanetary system (the exoplanet is resolved from the star). Under these circumstances, all of the geometric illumination unknowns (orbit radius, eccentricity, planet spin angular momentum direction, orbit angular momentum direction, orbit and planet spin periods and phases) reduce to only four unknowns: two angles of the exoplanet spin vector orientation, planet rotation period, and phase. The phase is arbitrary, and the period is easily obtained from the exoplanet integrated light curve, leaving just two planet spin geometry parameters to be

obtained from light-curve inversion. While not all of the orbital parameters will always be obtained with high sensitivity using direct imaging, we show how more than just the planet spin parameters and period can be obtained from light-curve inversions. Our inversion solutions are based on a coordinate system that describes the planet spin in terms of its angle with respect to the line-of-sight direction and its azimuth around this direction.

With the independent formalism presented in this paper—ExoPlanet Surface Imaging (EPSI)—we confirm some of the conclusions of earlier papers and elaborate further applications for planets with and without clouds and with seasonal variations, photosynthetic organism colonies, and artificial structures built by advanced civilizations. Multiwavelength observations of such planets may enable detection of primitive and even advanced exolife. Cowan et al. (2009) demonstrated longitudinal inversion information (with an assumption that latitudinal information could also be extracted). Our inversions demonstrate real surface "mapping" with latitudinal and longitudinal information. Also, in contrast to Fujii & Kawahara (2012), our modeling suggests that large ground-based telescopes with achievable wavefront control will be able to infer surface albedo maps. For example, mapping Proxima b could be done with a 12 m diameter terrestrial telescope. Hence, this paper focuses on realistic models and expectations for mapping the nearest exoplanets.

We show that moderate signal-to-noise ratio (S/N) time-series photometry of an exoplanet's reflected light can yield a 2D surface map of its albedo using an inversion technique. Reflected light photometry (and/or polarimetry) of exoplanets when the planet rotation axis is inclined with respect to the orbit plane normal direction offers the greatest possibility for mapping the exoplanet surface or seeing stable atmospheric structure with surprisingly high spatial resolution. Our numerical technique follows similar algorithms used for mapping starspots (Berdyugina 1998; Berdyugina et al. 1998, 2002).

The recent discovery of the nearest exoplanet, Proxima b (Anglada-Escudé et al. 2016), is an opportunity for obtaining the first surface (and/or weather) images of a possibly Earth-like exoplanet. Here we investigate in some detail the orbit-rotation parameter space relevant to Proxima b. We estimate the necessary S/N of the data and evaluate how it can be achieved with future telescopes.

The paper is structured as follows. In Section 2, we describe our direct model and an inversion algorithm. In Section 3, we present simulations and inversions for exoplanets with Earth-like albedo distribution due to ocean and land topography. We show that, under some circumstances, there is sufficient information in the reflected light curve to resolve an accurate map of the exoplanet surface on the scale of subcontinents. We also discuss limitations due to data noise, weather system evolution, and seasonal variations in the cloud and surface albedo. In Section 4, we present inversions for solar system planets and moons as analogs of exoplanets. We can recover global circulation cloud patterns on Jupiter, Neptune, and Venus, as well as surface features on the Moon, Mars, Io, and Pluto. In Section 5, we present models for spectral (broadband) imaging of exoplanets with Earth-like life and demonstrate that photosynthetic biosignatures and surface composition can be unambiguously detected with our technique. We also model hypothetical planets with global artificial structures (techno-signatures) that can be detected under certain circumstances. In Section 6, we present simulations and inversions for the Proxima b planet assuming tidally locked orbits at the 1:1 and 2:3 resonances. In Section 7, we investigate and formulate observational requirements for the telescope size and scattered light level in order to obtain spectral images of Proxima b and possible rocky planets in the stellar system nearest to the Sun, Alpha Centauri A and B. We find that telescopes with diameters of 12 m or larger and with a high level of scattered light suppression can achieve the required S/N in planet brightness measurements above the stellar glare background. We also estimate how many Earth-size and super-Earth planets in the water-based habitable zones (WHZs) of the nearby 3500 AFGKM stars can be imaged with the EPSI technique depending on the telescope aperture for a given scattered light background. Finally, in Section 8, we summarize our results and conclusions.

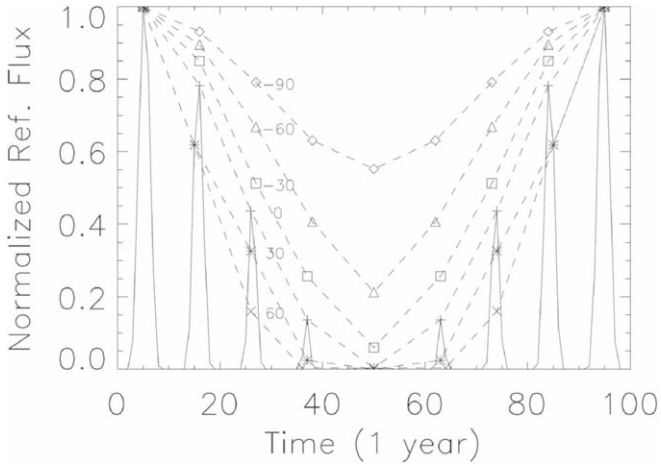

Figure 1. Reflected light curves for an exoplanet with a single high-albedo spot as a Gaussian with a width of about 5°. The planet has an orbit period of 100 time units, with a diurnal period of 10. The solid curve shows the light curve for an equatorial spot that goes in and out of view due to axial rotation and is illuminated fully or in part due to orbital motion. For spots on other latitudes, the peak amplitudes are changed. Symbols joined by dashed lines show the corresponding peak brightness for a spot located at the marked planetary latitudes. The observer here is located 90° from the planet rotation axis, and the normal to the plane of the orbit is 45° from the rotation axis. These calculations assume a simple $\cos\theta$ albedo angle dependence.

2. Model and Inversion Algorithms

In this section, we describe the model and inversion algorithm. The model includes radiation physics and star–planet geometry. The inversion algorithm includes criteria for choosing a unique solution and evaluating the quality of the recovered image.

The concept of our EPSI technique is evident if we consider a set of high-albedo spots at fixed longitude but variable latitude. Figure 1 shows how the latitude information of each reflective spot is encoded in the yearly variation of the peak daily brightness. Each latitude creates a distinct yearly variation profile, while each longitude affects the light curve at a distinct daily temporal phase. It is evident that deprojecting corresponding daily phased brightness measurements over the course of an exoplanet year allows, in principle, reconstruction of the latitude and longitude albedo variation from orbital and rotational sampling.

In fact, assuming that the surface structure does not evolve (or does so insignificantly) during the time covered by the light curve, this information can be inverted into a 2D map of the

surface—an indirect imaging technique that is employed in various remote sensing applications, e.g., asteroid mapping (e.g., Kaasalainen et al. 1992) or stellar surface imaging (e.g., Berdyugina et al. 1998, 2002). Fujii & Kawahara (2012) employed this approach for exoplanets combined with the Tikhonov Regularization (TR) inversion algorithm, which minimized discrepancies between the model and observations by choosing the solution with the minimum albedo gradient; i.e., it results in the smoothest map solution. Here we describe an algorithm employing the Occamian approach (OA) inversion technique (Berdyugina 1998). It is based on principal component analysis, which does not constrain the solution with any prior specific smoothness properties (see Section 2.2).

2.1. Direct Modeling

2.1.1. Radiation Physics

The reflecting surface of the planet is divided by a grid in longitude and latitude. Each grid pixel is assigned a geometrical albedo value A for a given wavelength or passband and a phase function P defining the angular distribution of the reflected light. Thus, if P is defined, there are $N = N_{\rm lat} \times N_{\rm lon}$ unknowns, which comprise an albedo map of the planet with $N_{\rm lat}$ latitudes and $N_{\rm lon}$ longitudes. This generic description of the surface allows us to compute reflected light from various surfaces, including a cloud deck and the planet surface with and without an atmosphere.

Different phase functions can be assigned for different scatterers, e.g., Rayleigh for gas and small particles, Mie for cloud droplets, lab-measured bidirectional reflectance distribution function (BRDF) for various surfaces, etc. (e.g., Berdyugina et al. 2016; Berdyugina 2017). For simplicity, the initial tests presented in this paper were calculated with the assumption that surface reflection is isotropic; gaseous atmospheric scattering is Rayleigh, $\hat{\boldsymbol{P}}_{\rm Ray}$; and cloud particles are spherical droplets, $\hat{\boldsymbol{P}}_{\rm Mie}$, if not stated otherwise throughout the paper. In some cases, reflected flux spectra from dense (optically thick) high clouds can be described by a composite phase function including a Rayleigh scattering contribution from a thin gaseous atmosphere above the cloud deck and a diffuse but wavelength-dependent reflected flux from clouds of a given albedo $A_{\rm c}$. Hence, to account for clouds, we assume that each planet map pixel can have contributions from clouds and the planet surface, with respective filling factors $f_{\rm c}$ and $1-f_{\rm c}$. The corresponding gaseous atmosphere scattering contributions depend on the optical thickness of the atmosphere above the planet surface and cloud deck. Here we assume that the light scattered downward by clouds and subsequently reflected by the surface is trapped within the atmosphere and does not reach an external observer (i.e., one cannot "see" through clouds). This approach further simplifies the problem and accelerates inversions.

Multiple scattering is computed by iteratively solving the radiation transfer equations for intensity and polarization, i.e., for the Stokes vector $\boldsymbol{I} = (I, Q, U, V)^{\rm T}$ of a given frequency (omitted for clarity) toward the direction defined by two angles ($\mu = \cos\theta$, ψ),

$$\mu \frac{d\boldsymbol{I}(\tau, \mu, \psi)}{d\tau} = \boldsymbol{I}(\tau, \mu, \psi) - \boldsymbol{S}(\tau, \mu, \psi), \quad (1)$$

with the total source function

$$\boldsymbol{S}(\tau, \mu, \psi) = \frac{\kappa(\tau)\boldsymbol{B}(\tau) + \sigma(\tau)\boldsymbol{S}_{\rm sc}(\tau, \mu, \psi)}{\kappa(\tau) + \sigma(\tau)}, \quad (2)$$

where κ and σ are absorption and scattering opacities; $\boldsymbol{S}_{\rm sc}$ and $\boldsymbol{B}$ are the scattering source function and unpolarized thermal emission, respectively; and τ is the optical depth in the atmosphere with $\tau = 0$ at the top. The formal solution of Equation (1) is (e.g., Sobolev 1956)

$$\boldsymbol{I}(\tau, \mu, \psi) = \boldsymbol{I}(\tau_*, \mu, \psi) e^{-(\tau_* - \tau)/\mu} + \int_{\tau}^{\tau_*} \boldsymbol{S}(\tau', \mu, \psi) e^{-(\tau' - \tau)/\mu} \frac{d\tau'}{\mu}, \quad (3)$$

where τ_* is either the optical depth at the bottom of the atmosphere for the Stokes vector $\boldsymbol{I}^+(\tau, \mu, \psi)$ coming from the bottom to the top ($\theta < \pi/2$) or the optical depth at the top of the atmosphere ($\tau_* = 0$) for the Stokes vector $\boldsymbol{I}^-(\tau, \mu, \psi)$ coming from the top to the bottom ($\theta > \pi/2$).

The scattering source function $\boldsymbol{S}_{\rm sc}$ is expressed via the scattering phase matrix $\hat{\boldsymbol{P}}(\mu, \mu'; \psi, \psi')$, depending on the directions of the incident (μ', ψ') and scattered (μ, ψ) light:

$$\boldsymbol{S}_{\rm sc}(\tau, \mu, \psi) = \int \hat{\boldsymbol{P}}(\mu, \mu'; \psi, \psi') \boldsymbol{I}(\tau, \mu', \psi') \frac{d\Omega'}{4\pi}. \quad (4)$$

It has contributions from scattering both incident stellar light and intrinsic thermal emission. Their relative contributions depend on the frequency. For instance, for Rayleigh scattering, the intensity of the thermal emission of an Earth-like planet in the blue part of the spectrum is negligible compared to that of the scattered stellar light. The phase matrix $\hat{\boldsymbol{P}}(\mu, \mu'; \psi, \psi')$ is a 4×4 matrix with six independent parameters for scattering cases on particles with a symmetry (e.g., Hansen & Travis 1974). In this paper, we employ the Rayleigh and Mie scattering phase matrices, but our formalism is valid for other phase functions too.

The Stokes vector of the light emerging from the planetary atmosphere $\boldsymbol{I}(0, \mu, \psi)$ is obtained by iteratively integrating Equations (2) and (3) for a given vertical distribution of the temperature and opacity in a planetary atmosphere. We solve this problem under the following assumptions:

(1) the atmosphere is plane-parallel and static,
(2) the planet is spherically symmetric,
(3) stellar radiation can enter the planetary atmosphere from different angles and be polarized,
(4) an incoming photon is either absorbed or scattered according to opacities in the atmosphere,
(5) an absorbed photon does not alter the atmosphere (the model atmosphere includes thermodynamic effects of irradiation), and
(6) photons can be scattered multiple times until they escape the atmosphere or are absorbed.

These assumptions expand those in Fluri & Berdyugina (2010), namely that multiple scattering on both molecules and particles is accounted for, stellar irradiation can be polarized and vary with an incident angle, and the planetary atmosphere and surface can be inhomogeneous in both longitude and latitude. Boundary conditions are defined by stellar irradiation

at the top, surface reflection at the bottom, and planetary thermal radiation, if necessary. Note that the bottom boundary condition refers to reflection from both the planetary surface and the cloud deck. Depending on the structure of the phase matrix and the boundary conditions, the equations are solved for all or fewer Stokes vector components. Normally, it takes 3–15 iterations to achieve the required accuracy (depending on the surface albedo and optical thickness of the atmosphere).

The stellar light is initially approximated by blackbody radiation with the effective temperature of the star, but nothing prevents us from employing real stellar spectra. Theoretically, the stellar spectrum is removed by normalization to the incident light (like in the case of the solar system bodies). In reality, however, stellar spectral lines induce irradiation fluctuations and, hence, the S/N variations with wavelength. In Section 7 we show the realistic calculations of the S/N for the nearest exoplanet(s) in the Alpha Centauri system in broad photometric bands that are feasible in the near future.

For cloudless Earth-like planets, we used a standard Earth atmosphere (McClatchey et al. 1972), for which we computed Rayleigh scattering opacities and optical thickness depending on the height in the atmosphere. For cloudy planets, we assumed an atmosphere of a given optical thickness above the clouds, while the cloud particles scatter light according to the chosen phase function.

Using such atmospheres, we have computed reflected radiation for a set of incoming and outgoing angles. Since the amount of scattered light in a cloudless atmosphere depends on the surface albedo, we also computed the outgoing radiation for a set of surface albedo values. These precomputed sets were used for simulations and inversions of light curves. It is obvious that the optical thickness of the atmosphere influences the visibility of the surface. Therefore, for thicker atmospheres, there is less information in the light curve on the surface albedo, and this has to be accounted for while carrying out inversions. Time-dependent reflected light curves were computed by integrating local Stokes parameters over the planetary surface at different rotational and orbital phases. Various levels of Poisson (photon) noise were introduced into the theoretical light curves to imitate observations.

2.1.2. Star and Planet Geometry

If the planet is angularly resolved from the star by direct imaging with a large enough telescope, its flux can be measured directly. This also implies that the planet flux should exceed background stellar scattered light (including telescope scattering and sky background) at the angular separation between the planet and the star. If the star–planet system is unresolved, the stellar light is added to the planet reflected flux.

Since the stellar flux is generally variable (e.g., due to magnetic activity or oscillations) during the planet orbital period, it is important to have observing tools to disentangle planetary and stellar variability. In general, this is possible because (1) the starlight spectral and polarization characteristics are different from those of the planet, and (2) if the star is resolved from the planet, its variability can be separately measured.

We define the star–planet geometry in a Cartesian frame with the axis x toward the observer and y and z in the plane of the sky (Figure 2). The planet is assumed to rotate around its axis and orbits its star with different periods, P_r and P_o, respectively.

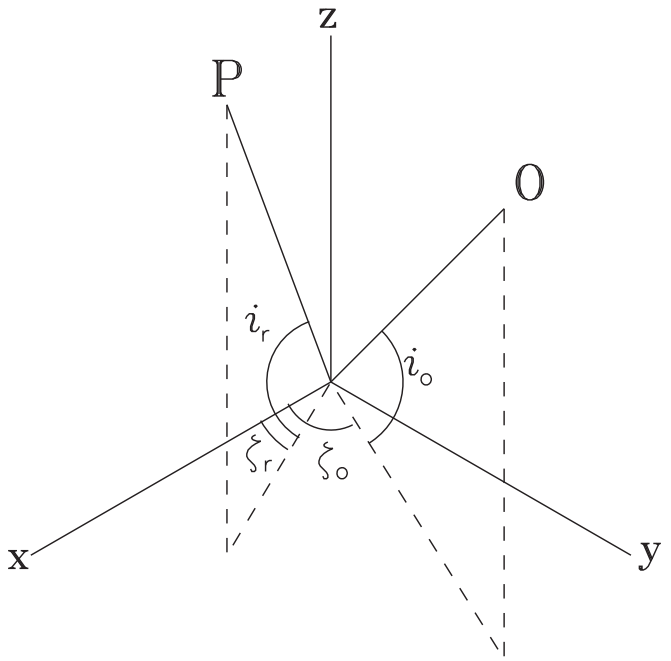

Figure 2. Geometry of a planet orbiting a star. The axes y and z are in the plane of the sky, and the x-axis is toward the observer. Planet axis inclination is i_r, planet axis azimuth is ζ_r, orbit normal inclination is i_o, and orbit normal azimuth is ζ_o.

The orientation of the rotational axis of the planet with respect to the observer can be generally described with two angles: inclination i_r and azimuth ζ_r (Figure 2). Thus, the xyz location on the planet surface is transformed into $x'y'z'$ by rotation by the angle i_r around the axis y and the angle ζ_r around the axis z. Here x' is the cosine of the angle between the local normal and the direction to the observer at a given phase, which defines the visibility function V: the pixel is visible to the observer if V is positive (i.e., $x' > 0$).

The normal direction to the orbit plane is also defined by the inclination angle toward the observer i_o and an azimuth angle ζ_o around axis z (within the xy-plane). To compute the amount of stellar illumination, we are interested in knowing the direction toward the star for any planet pixel at any given phase. We assume that the planet is far enough from the star to neglect the stellar solid angle; i.e., radiation coming from the star is unidirectional. Thus, the (x_o, y_o, z_o) direction to the star at a given orbital phase φ_o is transformed into $x'_o y'_o z'_o$ by rotations first by the angle i_o and then by the angle ζ_o (Figure 2). The cosine between the local normal to the planet surface and the direction toward the star in the observer reference frame defines the illumination function L: the pixel is illuminated by the star if L is positive, i.e., $x'x'_o + y'y'_o + z'z'_o > 0$.

The planet reflected flux for the given orbital and rotational phases is computed by integrating the intensity of the reflected light over the set of visible pixels weighted by the pixel area, albedo, and illumination fraction. For anisotropic reflection (scattering), it is also weighted by the phase function.

2.2. Inversion Algorithm

Recovering a planet surface albedo distribution from a time series of flux measurements requires solving an ill-posed

problem,

$$D = FS, \tag{5}$$

where D is a column vector containing M observations, S is a column vector containing N pixels on the planetary surface (in longitude and latitude), and F is the response operator expressed as an $N \times M$ matrix. The matrix F determines the transformation of a planet image into a data or model light curve. It includes all of the radiation physics and geometry described in the previous section. Thus, our task is to obtain the albedo map solution $\tilde{S}$ from the data D under the assumptions included in F by minimizing the discrepancy between the original data D and simulated data $\tilde{D} = F\tilde{S}$.

A simple inversion of the matrix F could provide an exact solution if $N = M$, but the solution will be noisy and unstable due to noise in the data. Alternatively, this problem can be solved (also for the case $N \neq M$) by maximizing the overall probability of obtaining the observed data (the likelihood function). However, to avoid fitting the data noise, the overall probability has to be reduced to some "reasonable" level, which leads to multiple possible solutions for a given probability (likelihood). The choice of the probability density function to calculate the likelihood function and the solution "goodness" criterion define the inversion algorithm and the solution itself.

Here we apply the OA algorithm that is inspired by the "Occam's razor" principle and has been employed for mapping stellar surface brightness from time series of both spectral line profiles and the stellar flux (e.g., Berdyugina et al. 1998, 2002). In contrast to the broadly used maximum entropy (ME) and Tikhonov regularization (TR) methods, the OA algorithm does not define an a priori quality of the solution, such as minimum information (ME) or maximum smoothness (TR). Instead, the OA chooses a solution $\tilde{S}$ with the information content equal to that in the data by means of a global maximization of the probability to fit the observed light curve D with the model $\tilde{D}$ using a minimum number of significant principal components (see details in Berdyugina 1998). This is the sole criterion for selecting the solution. We use the Poisson function to compute the likelihood function and the information content in the data because it is more suitable than the Gaussian function at lower S/Ns. In the following (Section 2.3), we also introduce new ways to characterize the inversion potential success depending on the geometrical and observational circumstances.

2.3. Inversion Quality

In this section, we define several solution quality measures after the solution $\tilde{S}$ has been obtained as explained in Section 2.2. This helps us to characterize the overall potential success of the inversion, which can be used to estimate and compare the efficiency of inversion algorithms, as well as to investigate potential biases in the resulting map due to uneven distribution of the information in the data, e.g., caused by observational constraints.

First, we define the inversion quality (IQ) parameter as follows. To compute it, we first transform an image S into a "binary" form using a threshold albedo, A_T (e.g., 0.1): $S(A \geqslant A_T) = 1$ and $S(A < A_T) = 0$. We do this for both the original (S) and recovered ($\tilde{S}$) images. This operation selects either bright or dark features in the images. Then, using these transformed images, we compute the IQ parameter percent as

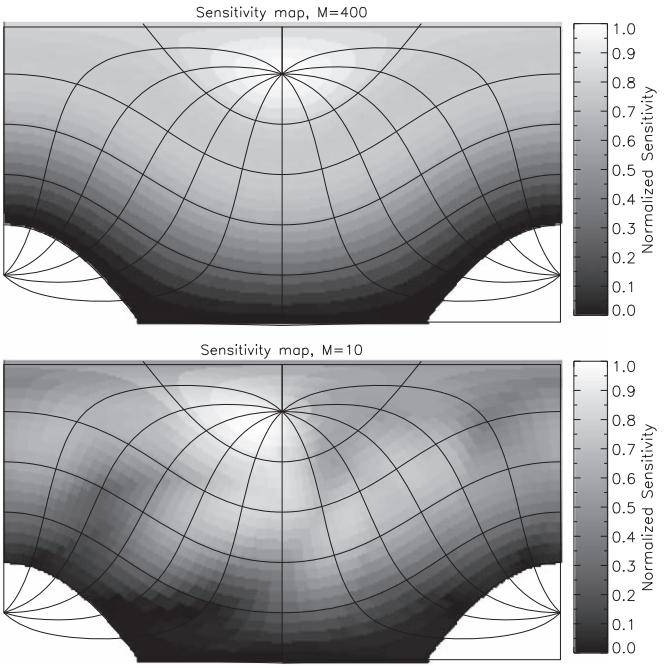

Figure 3. Sensitivity maps for model cases with large ($M = 400$) and small ($M = 10$) amounts of data. Observed phases are evenly distributed over the orbital period. The model geometry is the same as in Figure 2. A lack of measurements results in a "spotty" pattern of the sensitivity. Lower latitudes lack information because of a smaller projection area and sparse sampling.

follows:

$$\mathrm{IQ} = \frac{100\%}{N} \sum_{i=1}^{N} [S_i \tilde{S}_i + (1 - S_i)(1 - \tilde{S}_i)]. \tag{6}$$

Thus, IQ is the percentage of pixels in the recovered map having the albedo range coinciding with that in the original map. It is obvious that the IQ parameter depends on the chosen albedo threshold. We found, however, that for a successful inversion, IQ variations with the threshold near the center of the albedo value distribution are not large. In the following section, when discussing the inversion results, we will use the threshold albedo $A_T = 0.1$.

Another informative characteristic of the inversion success is the standard deviation (SD) of the recovered map with respect to the input map normalized to the maximum albedo and expressed in percent. This provides an overall measure of the map goodness for purpose of testing.

We also compute a sensitivity map in order to evaluate a relative distribution of the available information over the planetary surface. It is composed of products of the visibility and illumination functions summed over all observed phases,

$$\hat{S}_i = \sum_{j=1}^{M} V_{ij} L_{ij}, \tag{7}$$

where $i = 1$, and N runs over all planet pixels. Thus, $\hat{S}_i$ is proportional to the number of photons reflected toward the observer by the ith pixel during the total observing time, which defines the error of the restored pixel's albedo. In Figure 3, two sensitivity maps are shown for model cases with large and small amounts of data. When data sampling is sparse, large gaps in the sensitivity map become apparent. Since the geometry of the planetary orbit and the rotational axis direction

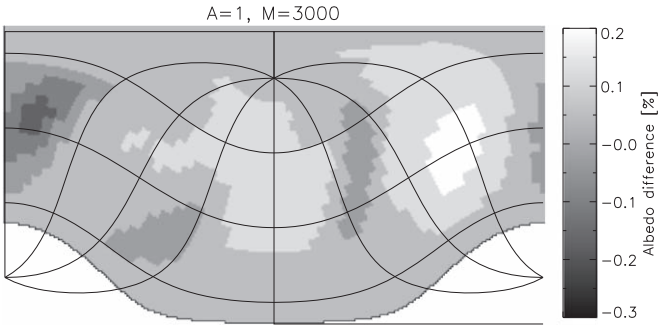

Figure 4. Distribution of deviations from the true albedo values $A = 1$ for a model with $i_r = 60°$, $\zeta_r = 0°$, $i_o = 30°$, and $\zeta_o = 60°$ shown in Figure 2 and $M = 3000$ as in models EN3000 and ES3000 (see Table 1).

with respect to the observer are fixed for a given exoplanet, the sensitivity map helps to optimize data sampling for the best inversion result.

One more way to characterize the quality of the recovered map is to carry out inversion of a light curve for a uniform albedo map (e.g., $A = 1$) with the same set of sampled phases and S/N as in the observed light curve. The resulting recovered map $\tilde{S}_1$ provides a distribution of expected deviations from the true albedo values for each pixel. These include limitations due to data sampling, visibility and illumination geometry, S/N, and the choice of the solution "goodness" criterion. Figure 4 shows an example inversion for the $A = 1$ map.

3. Exo-Earth Albedo Inversions

In this section, we present example simulations and inversions for an Earth-like planet with continents, oceans, and ice caps that allow for large albedo variations across the planetary surface. We demonstrate how the information encoded in the reflected light curve helps to resolve an accurate map of the exoplanet surface on the scale of continents. We also discuss limitations due to data noise, weather system evolution, and seasonal variations in the cloud and surface albedo. We characterize the inversion results with the quality parameters introduced in Section 2.3 and investigate how the quality can be maximized. We suggest that further improvements in the recovered image quality can be achieved by using polarized light curves in addition to the flux measurements. Such data may be useful for obtaining other local parameters, like the phase function.

In our tests, we vary the number of planet rotations per orbital period M_{rot} and the number of observed phases per planet rotation M_{ph}, as well as S/N, geometrical parameters, and cloud cover. As explained earlier, the total number of measurements is $M = M_{rot}M_{ph}$.

We employ monthly Earth maps produced by the *NASA Earth Observatory* (*NEO*) satellite missions (https://earthobservatory.nasa.gov/). The geometrical albedo maps with no clouds are used in Section 3.1. The effect of seasonal surface albedo variations is analyzed in Section 3.2. To study the effect of variable cloud cover, we analyzed a combination of the cloudless albedo maps and monthly cloud cover maps weighted by corresponding filling factors in Section 3.3.

We have rebinned the maps to the $6° \times 6°$ grid, simulated light curves, and carried out inversions as described in Section 2. The employed models are summarized in Table 1. If not mentioned otherwise, they are computed using the following geometrical parameters: $i_r = 60°$, $\zeta_r = 0°$, $i_o = 30°$, and $\zeta_o = 60°$. Inversions are solved for different combinations of these angles. This is practical when inversions are applied to partial orbit data, i.e., when orbital parameters may not be known with a sufficient accuracy from direct imaging measurements.

Table 1
Test Inversion Models for an Earth-like Planet

Model	M_{rot}	M_{ph}	S/N	IQ (%)	SD (%)
EN3000	60	50	200	89	10
ES3000	60	50	200	89	15
EN200	20	10	200	87	11
EN400	20	20	20	80	13

3.1. Cloudless Exo-Earths

First, we verify that we can resolve planet surface features in both longitude and latitude under favorable conditions; i.e., we assume data with sufficient S/N, a sufficient number of measurements, a favorable (but not unlikely) planet geometry, an optically thin (at a given wavelength) atmosphere, and no clouds. Inversions for less favorable scenarios are presented in subsequent subsections. We use the $6° \times 6°$ surface grid for inversions, as it yields reasonable surface resolution and a comfortable computational effort. This grid has $N = 1800$ pixels (when $i_r = 90°$), which implies that the measurement number M should be of the same order for a realistic solution. We note that our algorithm also converges when $N > M$, but errors increase.

For the first test, we assume that it is possible to obtain planet brightness measurements at 50 evenly spaced axial rotational phases with an S/N = 200. The orbital period is assumed to be equal to 60 planetary rotations, resulting in a total of $M = 3000$ measurements. This case may be representative of an Earth-like planet in a WHZ of K–M dwarfs. As two relevant examples, we carry out inversions for a planet with terrestrial geography visible from either the north or south poles: models EN3000 and ES3000. Here we used the albedo map for 2003 March, which shows some snow fields on the northernmost landmasses and large areas of green vegetation.

The inversion results for these models are shown in Figures 5 and 6, respectively. They successfully recover about 90% of the continental landmass with $A > 0.1$ and a relative SD of 10%–15%. The shape of the continents and their large-scale albedo features (subcontinents) are resolved on the scale of Australia and the Sahara. This demonstrates the power of our algorithm.

To investigate the sensitivity of the IQ to the geometrical parameters, we have simulated a grid of models over a range of planet axial and orbital inclinations. The inversion results for these models are summarized graphically in Figure 7. The plots show the dependence of the IQ (Equation (6)) and SD parameters on the inclination angles. Overall, our inversion algorithm performs very well at a large range of inclination angles, except for their extreme values: the median values of IQ and SD are 86% and 12%, respectively. At a higher planet axis inclination ($\geqslant 80°$), it becomes more difficult to distinguish between the upper and lower planet hemispheres. A combination of low i_r with high i_o (like Uranus in the solar system seen on a near edge-on orbit) is also not favorable for rotational

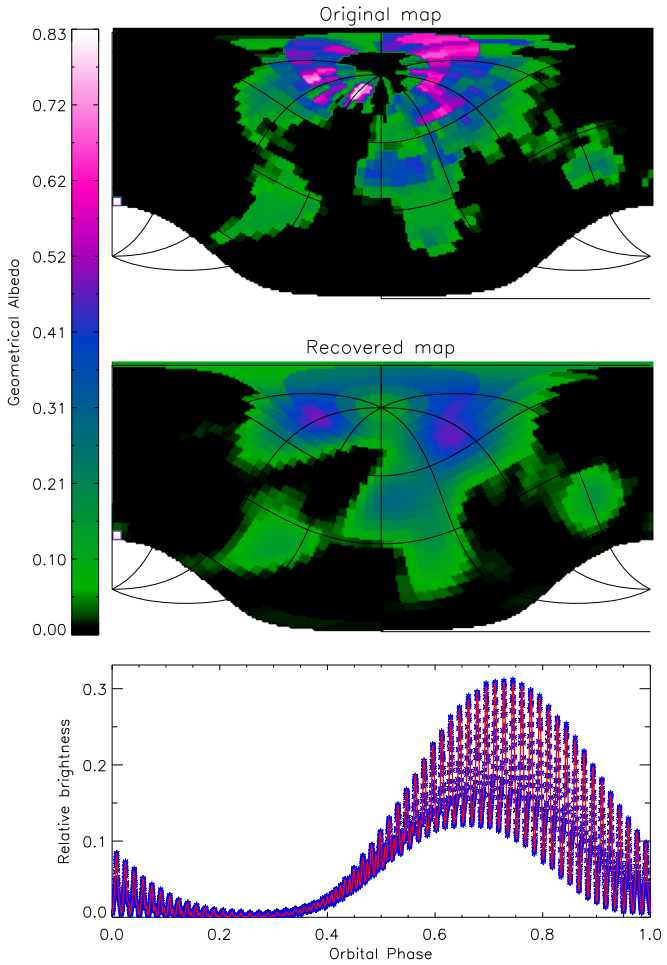

Figure 5. Original (top, for 2003 March) and recovered (middle) albedo map and light curve (bottom) for model EN3000 (see Table 1). The original map is used to simulate the "observed" light curve (blue symbols). The solid red line light curve is the best-fit model corresponding to the recovered map. The error bars of the simulated data are smaller than the symbol size.

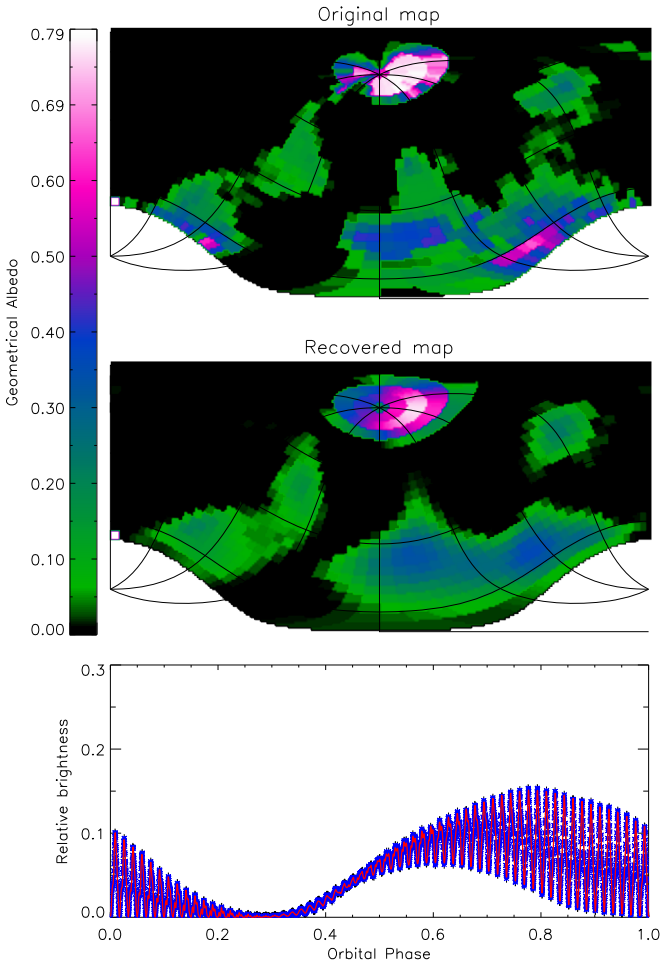

Figure 6. Same as Figure 5 but for model ES3000.

surface imaging. However, if both i_r are i_o are low, rotational modulation still produces enough signal for a reasonable inversion. There is a particularly favorable combination—a "sweet spot"—where inversions are most successful due to a good variety of geometrical constraints on visibility and illumination of pixels: near $i_r = 50°$–$70°$ and i_o of $30°$–$70°$.

3.2. Seasonal Variations

When the planet rotational axis is inclined with respect to the orbital plane, like for the Earth, one can expect seasonal reflected light fluctuations due to varying snow, cloud, and biomass surface cover. In this section, we analyze light curves generated from a series of monthly Earth albedo maps but yet without clouds. We consider two ways to evaluate this effect.

First, we combine 12 subsequent monthly maps (for 2003) and carry out inversion of a year-long light curve. Hence, seasonal variations are treated as systematic noise, and the inversion delivers an average planet albedo map. This map should be compared with the average of the 12 input maps weighted by the illumination fraction. Such weighting is necessary because the solution will be dominated by maps seen near the maximum illumination phase (i.e., near the maximum brightness of the light curve). The result of this test is shown in Figure 8, with the same planet parameters as for the EN3000 model. As expected, the quality of the restored map is reduced because of unaccounted systematic differences in the simulated and best-fit light curves.

The second test is to use the same simulated input as in the first test but to carry out inversions on parts of the light curve. With a sufficient number of measurements, one can infer maps for different orbital phases and investigate season progression on the planet. If such variations are found, they may help to constrain the inclination of the rotational axis of the planet. The results of such tests are shown in Figure 9. The quality is obviously reduced as compared to the EN3000 model because of the smaller amount of data. In addition, only parts of the planet surface could be inferred because of limiting illumination at particular orbital phases. However, this exercise demonstrates that useful information on the planet surface structures can be obtained even from partial light-curve inversions.

3.3. Partially Cloudy Exo-Earths

Planets with liquid water on the surface will most likely experience a water cycle as on the Earth. This implies that clouds will be forming seasonally and sporadically, creating various weather conditions. To investigate how the information content in the recovered exoplanet albedo map depends on the cloud cover, we have computed several cases with various cloud coverages.

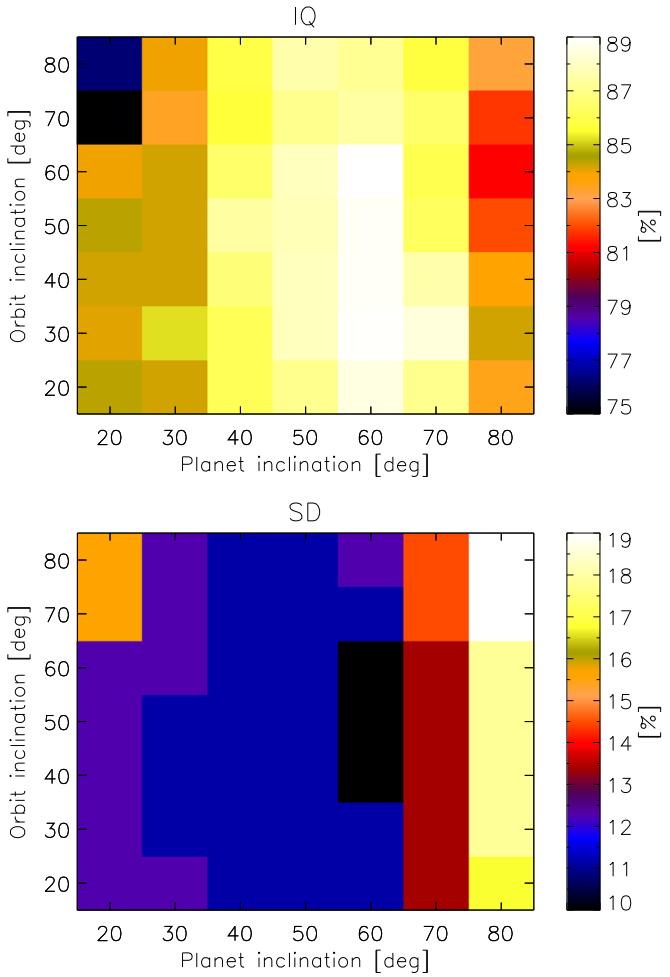

Figure 7. Dependence of the IQ parameter (Equation (6)) and map SD on the planet and orbit inclination angles i_r and i_o for model EN3000. The median values of IQ and SD are 86% and 12%.

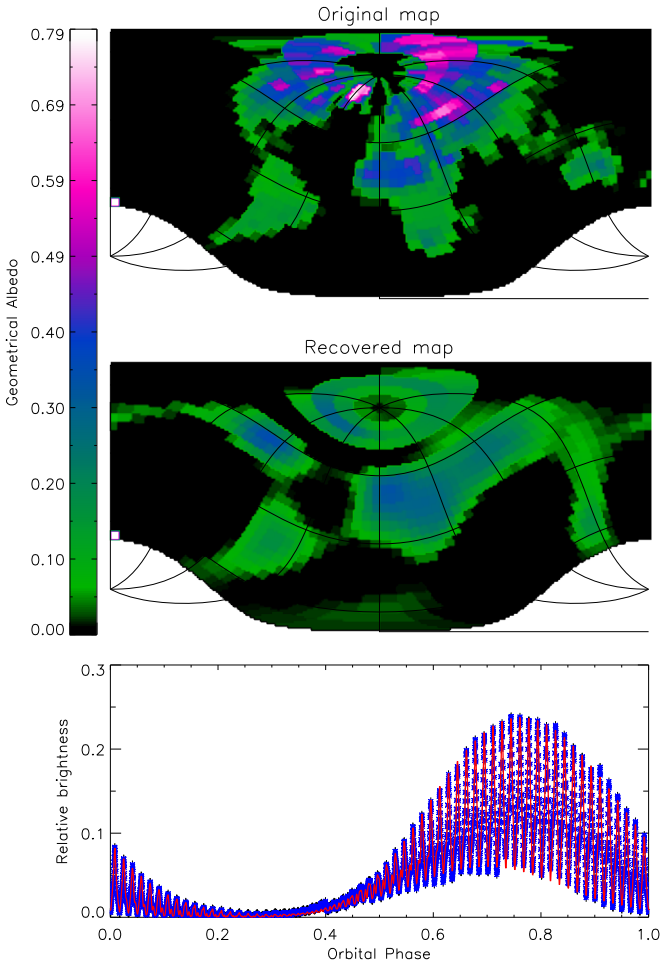

Figure 8. Seasonal variation effects in a year-long light curve. Top: weighted average of the 12 input albedo maps for 2003. Middle: recovered average albedo maps. Bottom: simulated (crosses) and best-fit (line) light curves. The error bars of the simulated data are smaller than the symbol size, and IQ = 84%, SD = 11%.

As in Section 3.2, we have combined 12 subsequent monthly maps for 2003 and augmented them with corresponding monthly cloud cover maps (also from the *NEO* website). The cloud maps were considered as masks, with each pixel being the cloud filling factor f_c. The filling factor of the cloudless surface was correspondingly reduced by the factor $1 - f_c$. In addition, we have scaled the cloud cover by a global factor in order to quantify how the optical thickness of the clouds affects our ability to see the planet surface. As indicated above, the recovered map is to be compared with the average of the 12 input maps (with seasonal variations of both the surface albedo and cloud cover) weighted by the illumination fraction. Two test results are shown in Figure 10, with the same planet parameters as for the EN3000 model and global scaling of cloud coverage by factors of 0.1 and 0.3. As expected, the quality of the restored planet surface albedo maps is significantly reduced for heavily clouded planets. However, longer series of measurements should reveal high-contrast surface features in more detail.

If clouds dominate the planet albedo, the cloud distribution and thickness can be detected on such planets. In this case, the rotational variation amplitude reduces, and the cloud light-curve signal approaches that of a homogeneous sphere, as shown in Figure 4. The recovered cloud distribution and thickness can provide additional constraints on the exoplanet climate and heat circulation in its atmosphere. The cloud physical and chemical composition can be retrieved with the help of polarization measurements as discussed in Section 3.6.

3.4. Limited Data Inversions

The inversion technique is surprisingly forgiving of S/N and the number of observation points. In this section, we investigate how inversions perform under less favorable conditions.

Here we compute the inversion with a reduced number of observations per planet rotation period, such as M_{rot} is reduced to 20 and M_{ph} is reduced to 10, and vice versa, when $M_{rot} = 10$ and $M_{ph} = 20$. Hence, the total number of measurements in both cases is 200, well below N (model EN200 in Table 1). The geometrical parameters are the same as before, and the original map is for 2003 March. Despite this difference in M_{rot} and M_{ph}, these two cases result in maps of similar quality. In Figure 11, we show one of these cases. It is only somewhat poorer as compared to the "ideal" inversion presented in Figure 5. The major part of the landmass is recovered with realistic albedo contrast (but without some details) with IQ = 87% and SD = 11%. We conclude that it is the total number of measurements, not necessarily the number of measurements

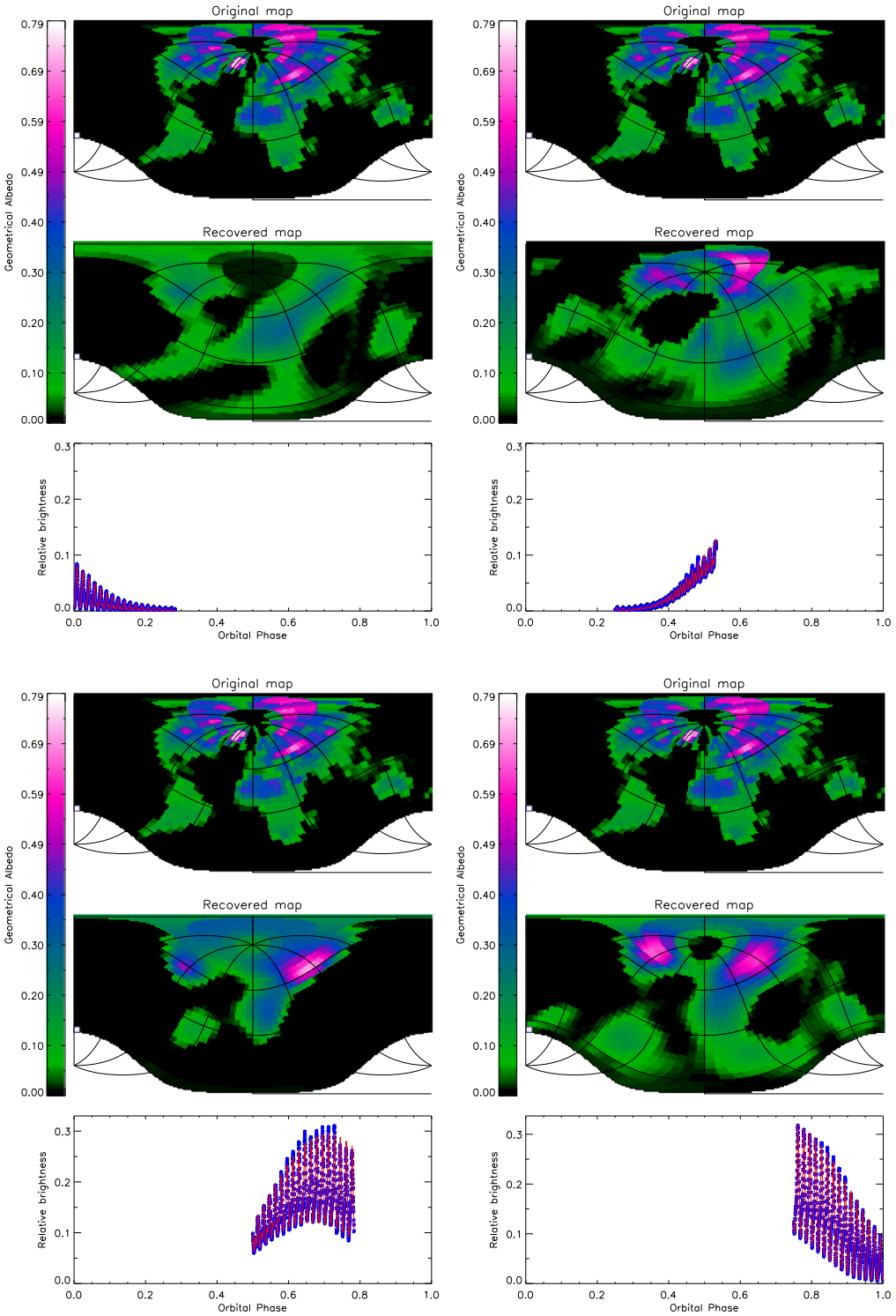

Figure 9. Same as Figure 8 but for 3 month light curves. Top left: months 1–3, IQ = 83%, SD = 17%. Top right: months 4–6, IQ = 82%, SD = 12%. Bottom left: months 7–9, IQ = 84%, SD = 13%. Bottom right: months 10–12, IQ = 89%, SD = 13%.

during a single exoplanet day, that encodes the latitudinal information.

It is also interesting to see how the measurement S/N affects the output images. The case for $M_{\rm rot} = M_{\rm ph} = 20$ and S/N = 20 is shown in Figure 12 (model EN400 in Table 1). Here the fraction of the recovered continent landmass is reduced to 80% and SD to 13%, and many details are missing. However, even with this low S/N, there is a high-contrast spatial structure that we could interpret as evidence of a continental water world.

3.5. Geometrical Parameter Retrieval

The light curve contains more information than just an albedo map or cloud cover. It strongly depends on the geometrical parameters of the system. Therefore, it is possible

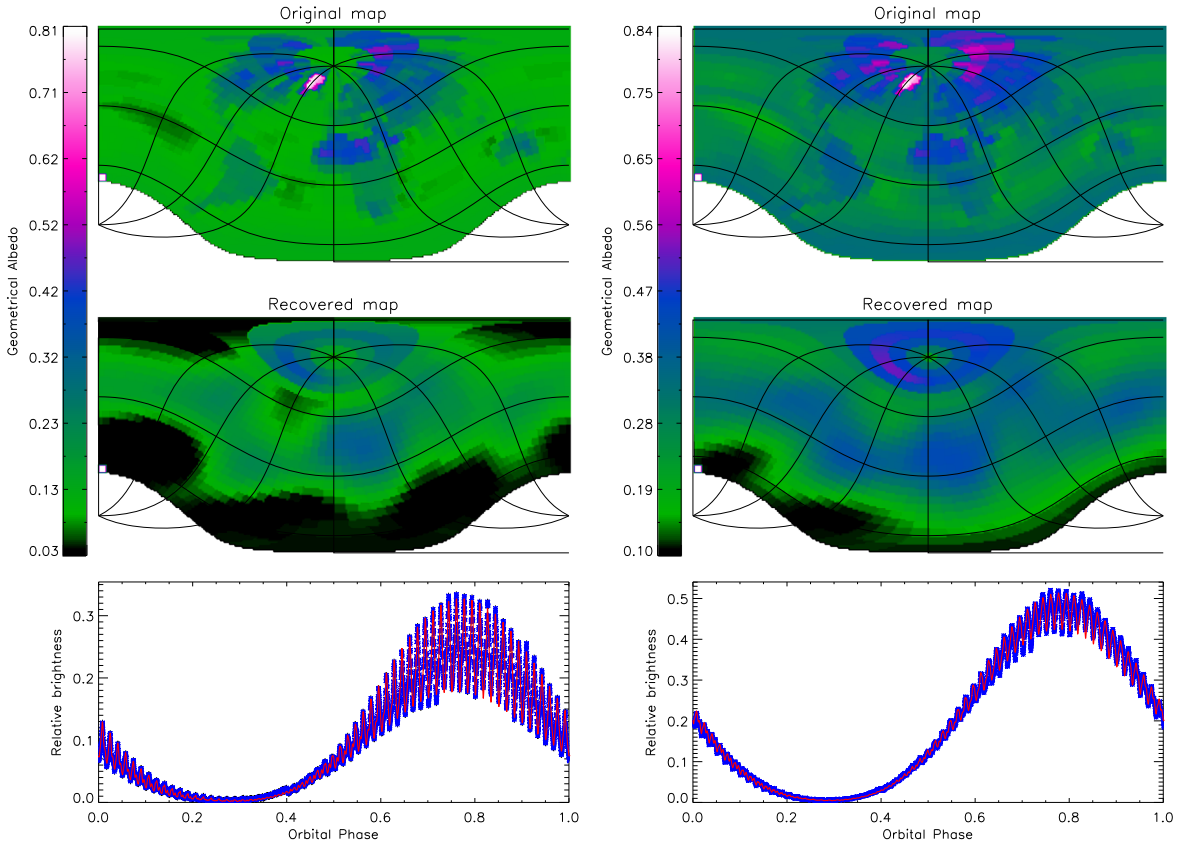

Figure 10. Same as Figure 8 but for the input maps including contributions from monthly cloud coverage maps. The global cloud cover has been reduced (as compared to the measurements on the Earth) by factors of 0.1 (left; IQ = 74%, SD = 10%) and 0.3 (right; IQ = 78%, SD = 13%).

to retrieve the albedo map, as well as the orbital and planetary axis angles i_o, ζ_o, and i_r.

Here we retrieve these angles by carrying out inversions and minimizing the discrepancy between the "observed" and modeled light curves within the angle domain. We have found that a high-S/N light curve (100 or more) allows for a quite accurate retrieval of the angles. An example for S/N = 200 is shown in Figure 13.

Obviously, noisier data yield weaker constraints on both the albedo map and angles. For instance, for S/N < 30, even if the albedo map can be reasonably retrieved, there is simply not enough information to create a surface map without independent information about the planet geometrical parameters. In fact, both the inclination and azimuth of the orbit can be evaluated from direct imaging data even in such noisier data if the planet is well resolved from the star. The planet's sky projected position with respect to the star changes over the course of its orbit, and the shape and orientation of this projected trajectory constrain the i_o and ζ_o angles, as well as its eccentricity (astrometric orbit). When this information is employed, the retrieval procedure can successfully converge to the true planet axis inclination angle, even at low S/Ns. An example of such a case is shown in Figure 14.

3.6. Polarized Reflected Light

With few assumptions, the reflected planetary light will be linearly polarized, in some cases at the 10% or larger level. From Earth-like planets, the light is polarized mostly due to scattering by molecules (Rayleigh), droplets or particles (clouds) in their atmospheres, or reflection from the land or ocean surface (Coffeen 1979). In contrast, the direct stellar light and instrument- and seeing-scattered starlight will have a much smaller linear polarization than the angularly resolved exoplanet—in many cases, smaller than 10^{-5}. We will consider linearly polarized light-curve inversions in detail in a future paper, but suffice it here to note that there is considerably more information in the polarized exoplanet light curves.

For example, the Stokes Q and U of the linearly polarized exoplanet light are sensitive to orbital parameters (Fluri & Berdyugina 2010) but eliminate the residual scattered starlight that generally contaminates the exoplanet photometry. Illumination variation due to, for example, elliptical orbits can also be accounted for in polarization inversion. Also, the mean component of the exoplanet rotationally modulated light polarization direction can provide the exoplanet's rotation axis inclination geometry independent of the details of the surface albedo map.

More interestingly, the exoplanet scattered light polarization angle is sensitive to the exoplanetary scatterer's latitude and longitude in a way that is completely independent from the corresponding unpolarized flux. This provides an additional constraint on the albedo map that is distinct from the seasonal and diurnal brightness variations.

Finally, reflection from the surface introduces polarized spectral features that can help to identify surface composition (Bréon et al. 2002) and biosignatures (Berdyugina et al. 2016). To distinguish true surface features from those of clouds, one has to use polarimetry simultaneously with flux measurements. In this case, it is possible to determine the scattering phase function, since polarization is strongly dependent on the

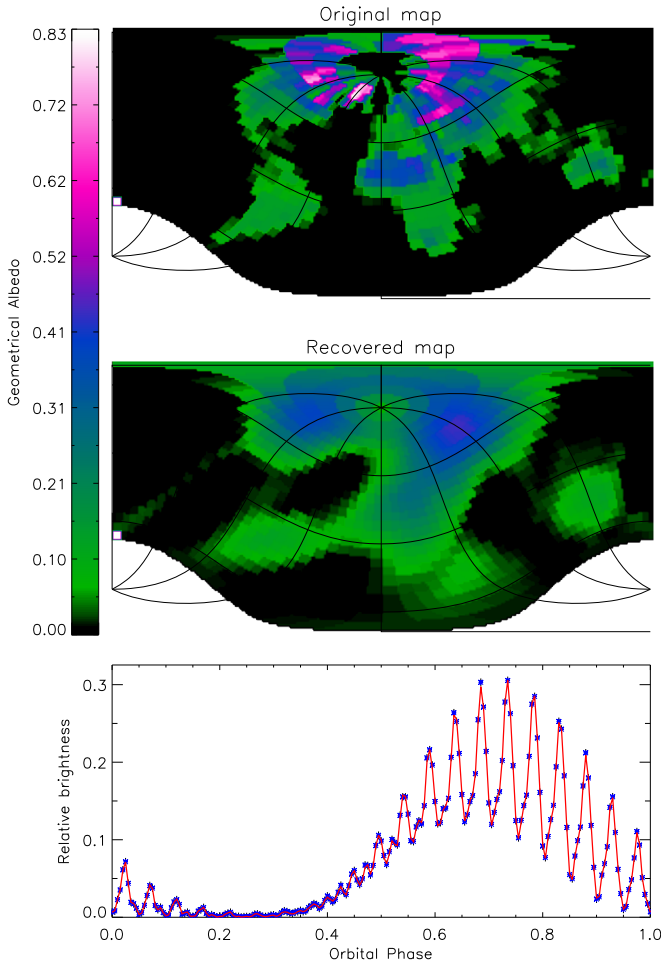

Figure 11. Same as Figure 5 but for model EN200: $M_{\rm rot} = 10$, $M_{\rm ph} = 20$, S/N = 200, IQ = 87%, SD = 11%.

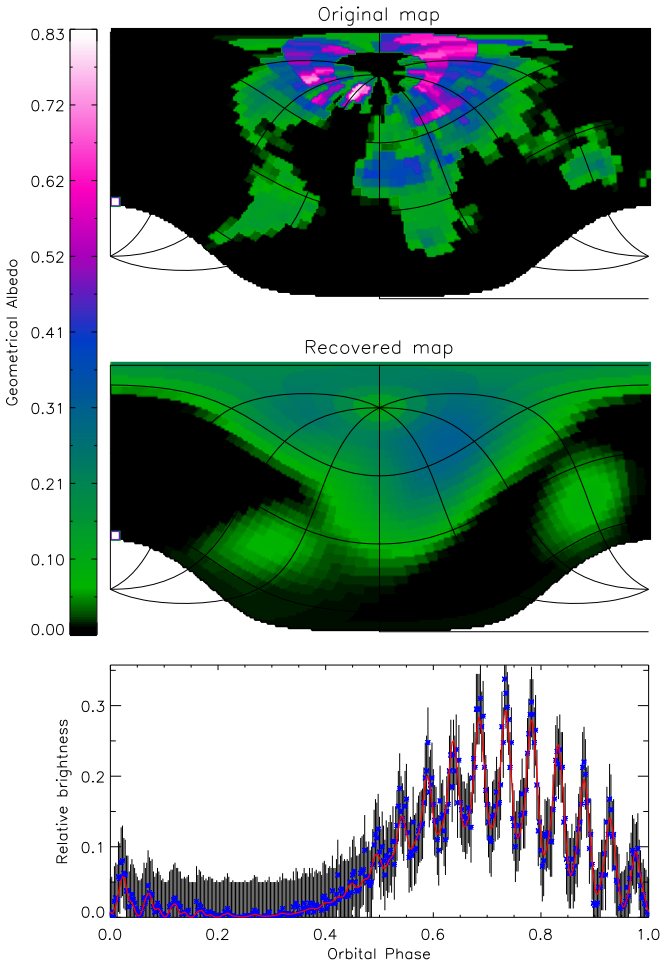

Figure 12. Same as Figure 5 but for model EN400: $M_{\rm rot} = M_{\rm ph} = 20$, S/N = 20, IQ = 80%, SD = 13%. Error bars of the simulated data are shown with vertical lines.

scattering angle and properties of scatterers (cloud particles, surface fine structure, vegetation, rocks, etc.).

While leaving the subject of polarized light-curve inversion for another paper, we expect that using polarized light will improve the sensitivity and allow inversion for other atmospheric and surface properties.

4. Solar System Albedo Inversions

In this section, we present inversions for some of the solar system planets and moons as analogs of exoplanets. We demonstrate how our EPSI technique can recover global circulation cloud patterns, as well as solid surface features without a surrounding low-albedo ocean.

For our tests, we employ high-resolution composite "photographs" of planets and moons delivered by various space missions and telescopes. From each such true-color image, we extract three images for the red, green, and blue (RGB) bands. These images are normalized to the planet average visible geometrical albedo. Then, corresponding RGB light curves are simulated and inverted. A composite image constructed from RGB recovered maps then allows for studying the chemical composition of spatially resolved surface features by means of low-resolution spectral analysis.

Our inversions in this section assume $M_{\rm rot} = 60$, $M_{\rm ph} = 50$, S/N = 200, $i_{\rm r} = 60°$, $\zeta_{\rm r} = 0°$, $i_{\rm o} = 30°$, and $\zeta_{\rm o} = 60°$. Only for Jupiter do we assume $i_{\rm r} = 30°$, so that its famous red spot is better visible.

4.1. Planets with Thick Clouds

Dense planetary atmospheres have vigorous circulation imprinted in their cloud pattern, like in zones, belts, vortices, jets, etc., on Jupiter, Saturn, Venus, etc. Three-dimensional models predict that similar patterns exist on exoplanets too (e.g., Heng & Showman 2015; Amundsen et al. 2016; Komacek & Showman 2016). Hence, images of solar system planets with clouds can be used as a good example for testing our inversion technique to map the albedo of planetary atmospheres with a thick cloud deck. In this section, we employ images of Jupiter, Neptune, and Venus for such tests. The original and recovered images (or their parts) for cloudy planets are shown in Figure 15. The details for each planet are presented in the following subsections.

We note that particles in dense clouds are usually larger than the wavelength of the optical light. Therefore, the Rayleigh approximation is not useful, and the Mie approximation is applicable only for spherical particles. In gas giants, such as Jupiter and Neptune, particles are generally nonspherical (ices) and require complicated phase functions. Therefore, the shape of their light curves is also affected by phase functions (e.g., Dyudina et al. 2016). In this section, for simplicity, when

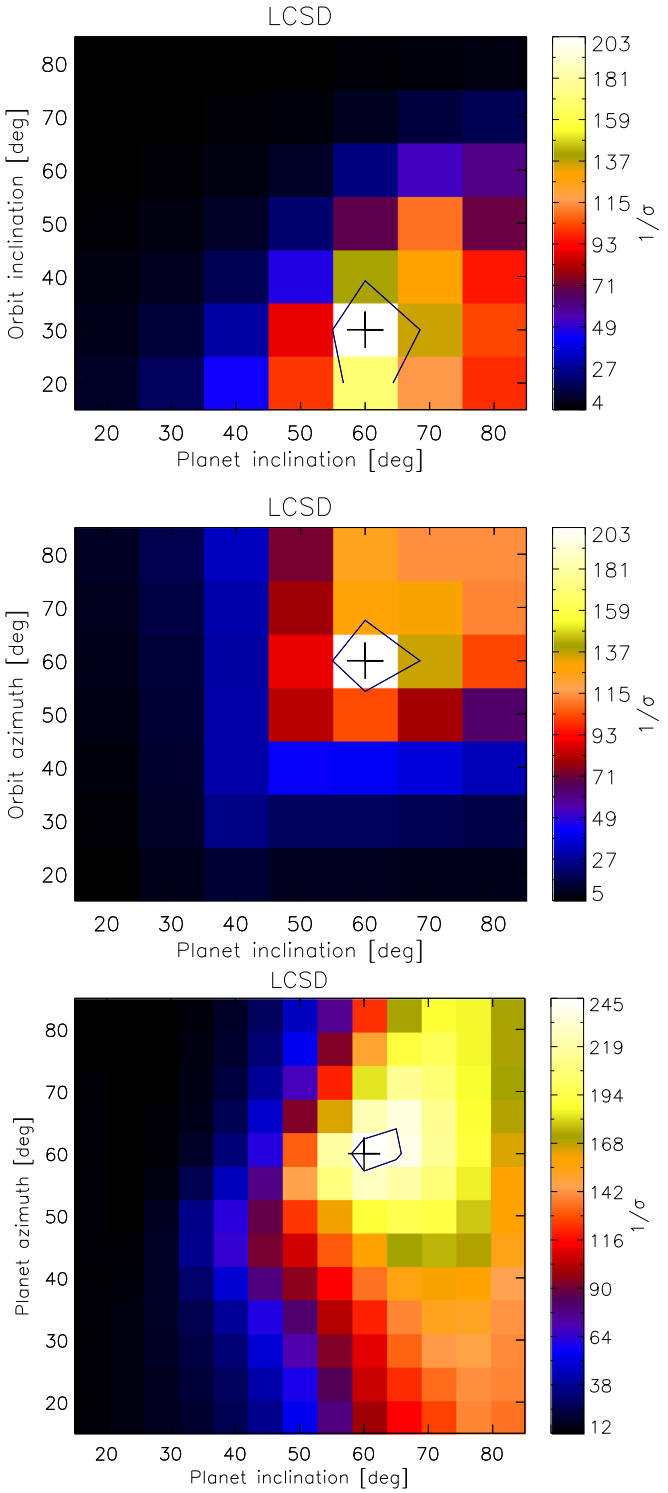

Figure 13. Retrievals of the angles i_o, i_r, ζ_o, and ζ_r for model EN3000 (S/N = 200) by minimizing the discrepancy between the "observed" and modeled light curves within the angles' domain. The plots show the inverse of the light-curve SDs. The true values of the angles are marked with crosses. Contours show 67% confidence levels.

generating flux light curves from cloudy solar system planets and applying inversions to them, we assume that clouds scatter isotropically with their geometrical albedo to be recovered by the inversion routine at different wavelengths. Thus, our first goal is to investigate how precisely low-contrast cloud structures can be recovered by the EPSI technique.

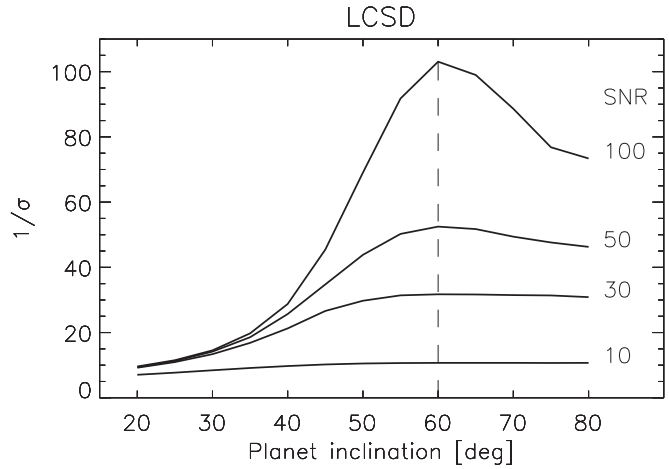

Figure 14. Retrievals of i_o only for model EN3000 with S/N = 10–100. The vertical axis shows the inverse of the light-curve SDs. The true value is marked with a dashed vertical line.

4.1.1. Jupiter

For Jupiter, we employ a global, high-resolution RGB map constructed using *Hubble* as part of the OPAL project (Simon et al. 2015). We have extracted from this image a part with bright zones and the Great Red Spot (GRS) within the latitudes of ±60° and longitudes of ±90°. Then, a full surface map from this part was constructed by rebinning it to the 6° × 6° grid for all longitudes and latitudes. The Jupiter average visible geometrical albedo is 0.52. Correspondingly, after normalization, the average albedos of the individual RGB images are about 0.6, 0.5, and 0.4, respectively. These are close to the measured values for Jupiter (Karkoschka 1994).

We have used this reduced, normalized, and rebinned RGB image for our inversions as an example of exoplanets with a global circulation cloud pattern. Also, we made it visible from the south pole, so that the GRS is well seen at higher latitudes. The GRS is well recovered, as well as the zones (bright clouds) and belts (dark clouds); see Figure 15. The overall result is very encouraging, since we can directly study the hydrodynamics of the thick atmospheres of Jupiter-like gas giants angularly resolved from their host stars with existing telescopes (see Section 7).

4.1.2. Neptune

We employ the RGB Neptune map obtained with the NASA *Voyager* mission, which discovered the Great Dark Spot (GDS) and traces of clouds at different heights in a highly windy atmosphere. Such spots (vortices) are long-lived but still transient features in the Neptune atmosphere. As for Jupiter, we used a part of the map with the GDS at a visible latitude. The optical geometrical albedo of Neptune is 0.41, but it is much brighter in the blue because of Rayleigh scattering and strong methane absorption in the red wavelengths.

The GDS is well recovered, but traces of clouds are below the reconstruction resolution (Figure 15). This example illustrates that blue planets may have transient vortices, which are detectable in a blue passband.

4.1.3. Venus Clouds

Venus is a cloud-enshrouded rocky planet, with clouds made of sulfuric acid droplets. It is possible that quite a few rocky

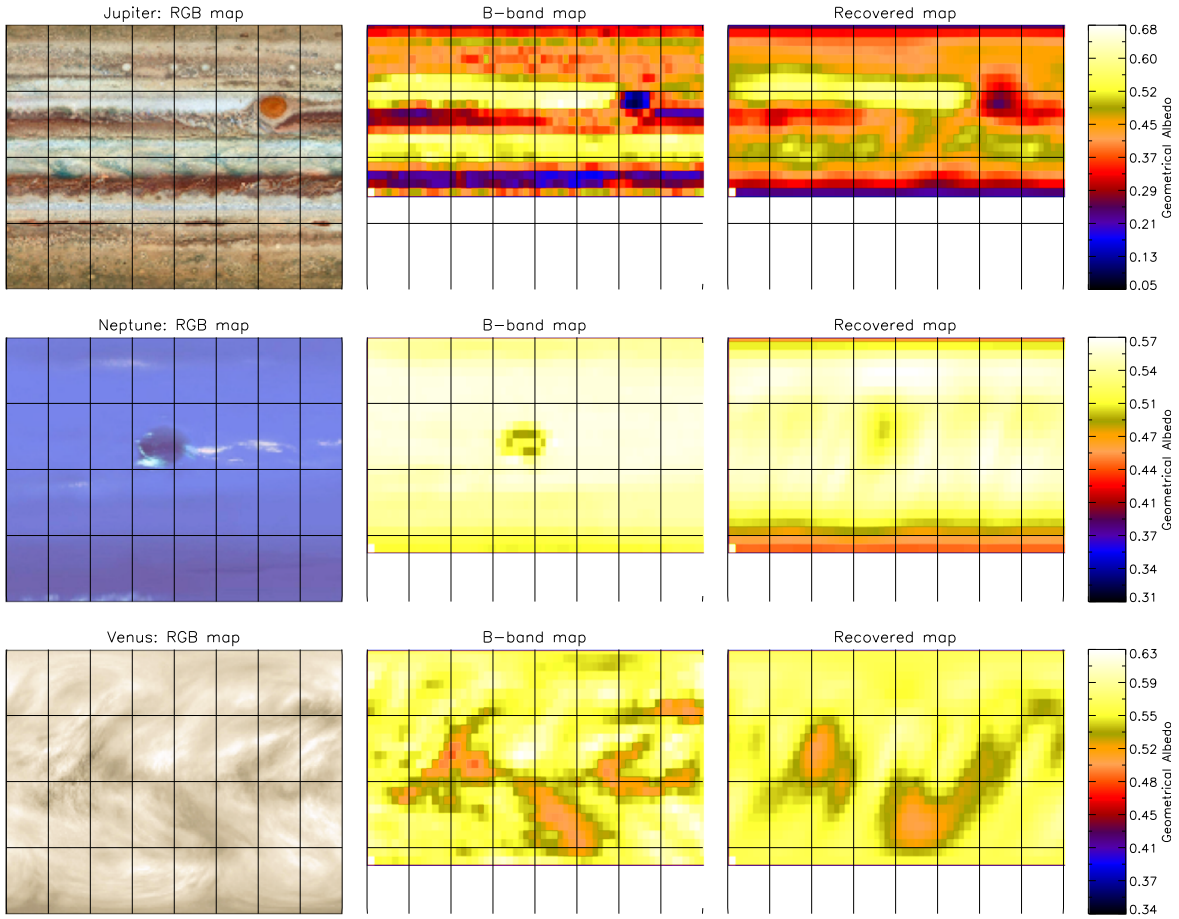

Figure 15. Albedo maps for the solar system planets with thick clouds. In the first column are original RGB maps of higher resolution, in the second column are original maps rebinned to the $6^\circ \times 6^\circ$ grid in a particular band, and in the third column are recovered maps in the same band. The original rebinned maps are used to simulate the "observed" light curve from which recovered images are obtained using inversions.

exoplanets at closer distances than the inner edge of the WHZ are as completely covered by clouds as Venus, with a strong greenhouse effect. Venus's upper clouds have a transient structure driven by fast winds (jets) in its atmosphere, so the entire atmosphere rotates in only four Earth days and in the opposite direction, as compared to the 243 Earth day surface rotation. We employed the RGB image of the Venus upper clouds obtained by the NASA *Galileo* spacecraft.

The Venus cloud optical geometrical albedo is very high: 0.69. The cloud structure on Venus is different from that on Jupiter, Neptune, and other gas giants (Figure 15). It is encouraging that our indirect imaging can distinguish between different cloud structures and provide insight into the global circulation of atmospheres on rocky and gas giant planets.

4.2. Solid Surfaces of Planets and Moons

For planets with transparent atmospheres or without atmospheres at all, we can recover images of their surface albedo variations, as we demonstrated above for the Earth. Here we look at several solar system planets and moons with interesting surface features. They generally reveal a history of meteoroid bombardment and geological (tectonic or volcanic) activity. Our results are compiled in Figure 16, and the details for each planet are presented in the following subsections. The solar system moons are used here only to illustrate how an exoplanet with similar surface features can be studied (detecting and imaging an exoplanet moon would generally require much larger telescopes).

4.2.1. Mars

Mars can be considered as an analog of cold rocky planets beyond the stellar WHZ. It has seasons, polar ice caps, and a very thin, transparent atmosphere, allowing a clear view of the planet surface in the optical. On the surface, there are volcanoes, canyons, and traces of earlier floods. Albedo features include sandy and dusty regions changing on a 10–100 yr scale, ice or frost, and polar ice caps varying with seasons. The optical geometrical albedo is quite low: 0.17. We employed an RGB map of Mars obtained by the NASA *Viking* missions. When rebinned to the $6^\circ \times 6^\circ$ grid, it still shows well the largest volcano in the solar system, Olympus Mons, as well as a large equatorial canyon system, Valles Marineris.

Shapes of dark dusty areas and bright highlands, including Olympus Mons, are well recovered in the *R*-band image. If the top of Olympus Mons was covered by snow, it would be quite conspicuous (see, for example, a reconstruction of volcanoes on Io in Section 4.2.4). Thus, seasonal variations of the albedo on exoplanets like Mars can be studied with EPSI.

4.2.2. Venus Surface

The Venus surface is not visible in the optical because of thick clouds. Its map is obtained using radar measurements.

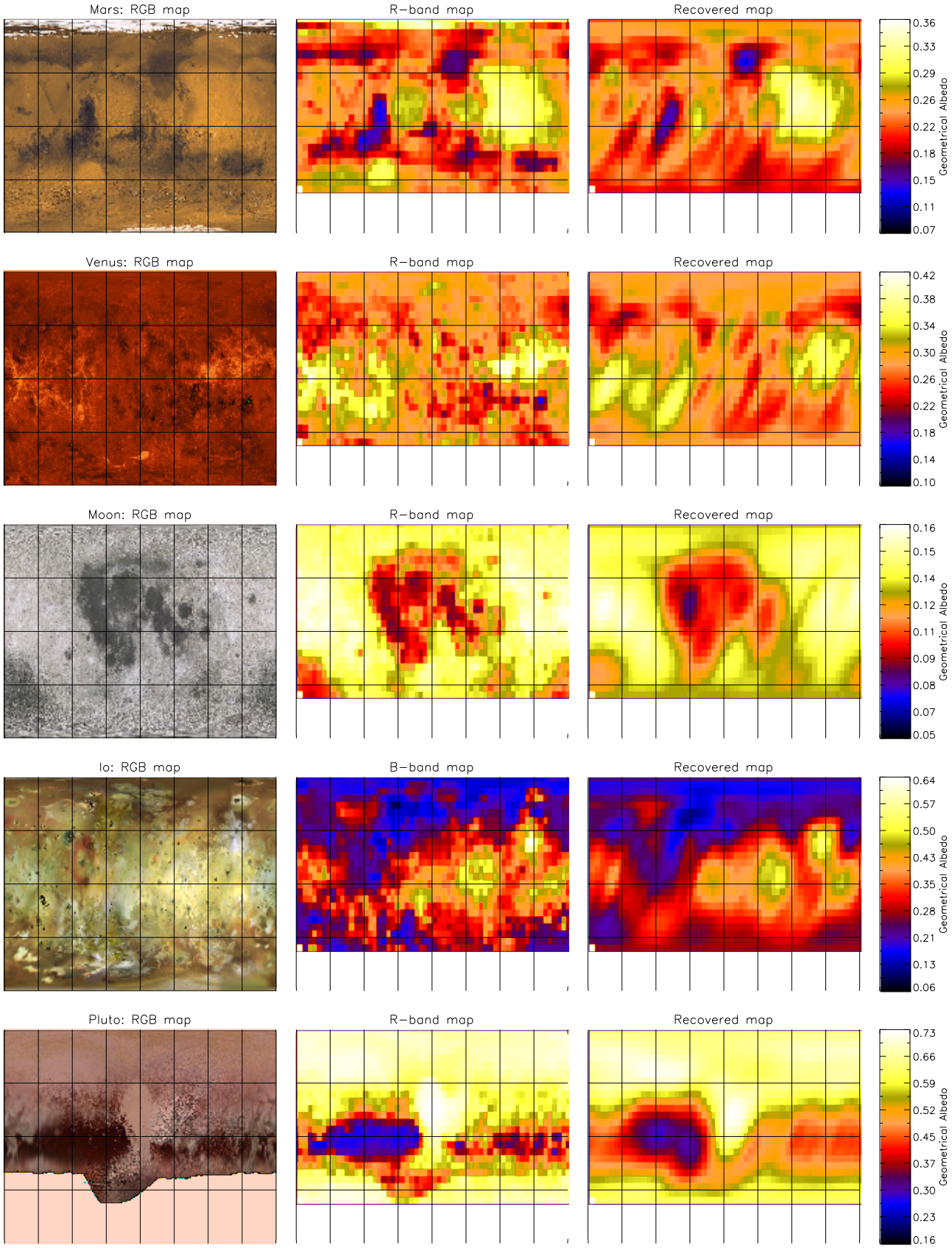

Figure 16. Albedo maps for surfaces of some solar system planets and moons. In the first column are original RGB maps of higher resolution, in the second column are original maps rebinned to the $6^\circ \times 6^\circ$ grid in a particular band, and in the third column are recovered maps in the same band. The original rebinned maps are used to simulate the "observed" light curve from which recovered images are obtained using inversions.

Under the clouds, the surface looks orange because red light passes through the atmosphere. The surface is hot, and structures are relatively small-scale because of regular resurfacing. Surface features include craters from large meteoroids (because only those can reach and impact the surface), multiple volcanoes, and some highlands. Since the albedo of these features is unknown, for our reconstruction, we have assumed that the overall surface optical albedo is the same as for Mercury, 0.14, which is similar to that of the Moon, whose highlands are lighter and lowlands are darker (e.g., filled with volcanic lava). We also assumed that the surface can be seen through a transparent atmosphere.

Variations of the albedo of different structures are quite well reconstructed, including large-scale dark and bright areas with some substructures. Volcanoes are quite small and are not resolved in the recovered image. However, if volcanic activity affected a larger area, that could be recovered (like on the Moon or Io; see the next section). Thus, time series of such indirect images of active exoplanets will allow for studying the volcanic activity and chemical composition of the new lava through multiband spectral imaging, as discussed for biosignatures and technosignatures in Section 5.

4.2.3. Moon

The Moon is an interesting analog of an exoplanet without an atmosphere. It is highly cratered, similar to Mercury, but it also has large areas of lighter highlands and darker maria filled with volcanic lava some billions of years ago. The light and dark areas have different composition. The optical albedo of the Moon is 0.12, similar to that of Mercury.

The overall shapes of the large-scale brighter and darker areas are well reconstructed. Such variety of the albedo on exoplanets without an atmosphere may help reveal the history of their formation and volcanic activity, as well as the composition of various areas.

4.2.4. Io

The Jupiter moon Io can be an analog of a very volcanically active exoplanet. Volcanic lava fills in impact craters and spreads over the surface, which is constantly renewed. The vivid surface colors of Io revealed by the NASA *Galileo* and *Voyager* missions are cased by silicates and various sulfurous compounds. In particular, volcanic plume deposits can be white, due to sulfur dioxide frost, or red, due to molecular sulfur.

We have employed a detailed RGB map of Io obtained by the *Galileo* mission. We made it visible from the south pole of the moon, so that interesting surface features are in view. The optical geometrical albedo used is 0.45. Large-scale, active volcanic areas are well reconstructed. In particular, the volcano Pele, distinguished by a large circular red plume deposit (in the upper left part of the map), is well seen in the recovered image. Bright volcanic slopes covered by sulfur dioxide frost, such as Tarsus R. (in the upper right part of the map), are also well recovered. We did not attempt it, but it seems possible that large volcanic plumes forming umbrella-shaped clouds of volcanic gases can also be detected with our imaging technique, if they last long enough.

Discovering and imaging such geologically active exoplanets will be valuable for studying their internal composition. Complementary images in the IR will help to determine the temperature and age of volcanic deposits.

4.2.5. Pluto

Pluto is an icy, rocky dwarf planet that may serve as an analog of exoplanets and planetesimals beyond the so-called frost line distance from the host star. The first albedo maps of Pluto obtained using light-curve inversion techniques (see Buie et al. 1997) revealed highly reflective features associated with recently replenished glaciers. Direct images of Pluto delivered by the NASA *New Horizons* mission have confirmed the presence of these spectacular glaciers of frozen methane, carbon monoxide, and nitrogen. Extended dark surface features are possibly due to tholins (Sagan & Khare 1979), which are common on the surfaces of icy outer solar system bodies and formed by UV or energetic particle irradiation of a mixture of nitrogen and methane. The surface of Pluto was found to have unexpected tectonic activity indicated by large craters with degradation and infill by cryomagma.

The optical geometrical albedo used in our simulations is 0.49. Since the *New Horizons* map of Pluto is incomplete, we assigned to the missing part a constant intermediate-value albedo. Also, we made the planet visible from the pole with a detailed map, so that the missing part is basically invisible with a given inclination angle. All large-scale structures, including the brightest glacier and tholin-rich areas, are well reconstructed. This is promising for detecting and studying cryovolcanic activity on icy exoplanets.

5. Biosignatures and Technosignatures

In this section, we present models for spectral (broadband) imaging of exoplanets, with the same parameters as in Section 4. We demonstrate that, for example, photosynthetic biosignatures and inorganic surface composition can be detected using EPSI. We also model hypothetical planets with global artificial structures that can be detected under certain circumstances.

5.1. Spectral Imaging of Biosignatures

Detecting biosignatures on exo-Earths is an ultimate goal of modern exoplanet studies. In most cases, this requires an analysis of the spectral content of the reflected, emitted, and/or absorbed flux from an exoplanet. For example, detecting spectral signatures of biogenic and/or out-of-equilibrium gases in exoplanetary atmospheres is a promising approach (e.g., Grenfell 2017; Catling et al. 2018; Kiang et al. 2018; Meadows et al. 2018; Schwieterman et al. 2018). Positive atmospheric detections will help select promising candidates, but definite conclusions for exolife detection will require complementary studies to exclude false positives.

Here we propose such a complementary approach using our surface imaging technique applied to exoplanet light curves measured in several spectral bands or using an efficient spectrograph. We show in this section that a "true"-color map of exoplanets inferred with our surface imaging technique could provide a powerful tool for detecting surface-based living organisms, in particular photosynthetic organisms that have dominated the Earth for billions of years.

We test our approach using a composite RGB image of Earth's surface samples: ice polar caps, ocean reflecting blue sky, deserts, and forest. This image is shown in Figure 17 (top

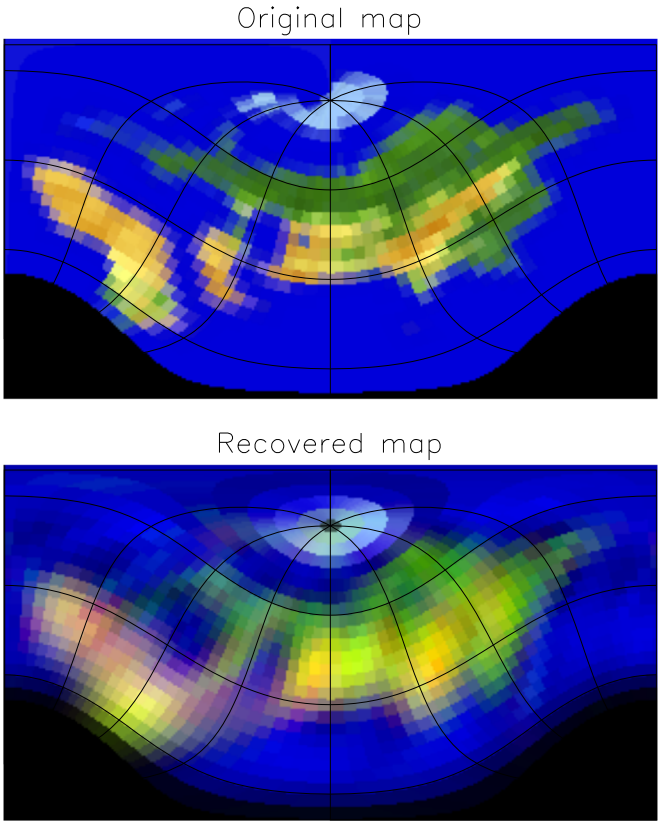

Figure 17. The RGB composite original and recovered maps of an exo-Earth with continents, oceans, and a polar cap. Continents are in part are covered by green photosynthetic organisms and in part by deserts.

panel). We complement this RGB image with a near-IR (NIR) image (0.75–0.85 μm) using our laboratory study of various organic and inorganic samples (Berdyugina et al. 2016). In particular, the most striking feature of the IR image is high reflectance by the green vegetation.

We have carried out inversions of the four RGB+NIR images separately and obtained recovered images as described in this paper. The input and output images are shown in Figure 18. Under favorable observing conditions, the quality of the recovered images is quite good. When combined in a true-color photograph, the recovered RGB image quite remarkably outlines the polar ice cap and continents with large desert and vegetation areas (see Figure 17; bottom panel).

By resolving surface features, spectra of various areas can be extracted and explored for life signatures. An example average spectrum of a small green area at midlatitudes in the eastern part of the planet is shown in the left panel of Figure 19 for both the input and recovered images. A geographically resolved spectrum with a deep absorption in the visible and high albedo in the NIR has been recovered very well. It quite strikingly reveals the presence of chlorophyll-rich organisms with the distinct red-edge signature typical of green plants and cyanobacteria. Thus, using spatially resolved images of exoplanets dramatically increases our chances to detect exolife, because we can carry out a spectral analysis of areas with high concentrations of living organisms, which is necessary for unambiguous detection (see models with various biopigments in Berdyugina et al. 2016).

In the right panel of Figure 19, we show an example spectrum of a desert area whose composition can be recovered using spectra of various minerals.

5.2. Technosignatures of Advanced Civilizations

A search for technosignatures of alien civilizations has been mainly focused on electromagnetic (radio, optical, IR) communication signals (e.g., Tarter et al. 2010; Adhikari et al. 2018; Angerhausen et al. 2018). However, a large variety of other technosignatures have been proposed (Berdyugina et al. 2018a).

The EPSI technique is capable of detecting such technosignatures as artificial megastructures (AMSs) constructed by advanced civilizations either on the surface or in the near space of an exoplanet. We consider AMSs to be of some "recognizable" shape and/or homogeneous albedo and most likely "geostationary." We have previously described how the thermal footprint of a civilization only slightly more advanced than that of Earth could be detectable at IR wavelengths from its planetary rotation signature (Kuhn & Berdyugina 2015). Since advanced civilizations would depend on stellar power sources to avoid planetary warming, it is likely that the low-albedo stellar energy collectors should be detectable using the mapping technique described here.

One example of such low-albedo installations is similar to our photovoltaic systems on the Earth's surface and in space. Such structures would absorb stellar light with high efficiency in particular spectral bands. In fact, the spectral signatures of such alien photovoltaics could be of similar shapes to those of various biopigments (see Figure 19 and Berdyugina et al. 2016), depending on the alien technology, energy needs, and available stellar light before or after it passes through the planetary atmosphere.

Another example would be high-albedo installations, also on the surface or in the near space, in order to redirect the incident stellar light, e.g., for heat mitigation by reflecting the light back to space. Such installations may reflect only a particular part of the spectrum, because the amount of the reflected energy can be regulated by both the size of the structure and the width of the spectral band.

We have simulated examples of exoplanets with AMSs of high and low albedo combined with the natural environment, similar to the Earth. Light curves were simulated in the RGB passbands and inverted separately, as described in previous sections for natural albedo variations. The final images were obtained by combining the individual RGB light-curve images into true-color images.

Our model AMSs are shown in Figures 20 and 21, imitating a photovoltaic-like power plant in space, above clouds, and urban-like areas under reflective "umbrellas" on a planet surface under a cloudless atmosphere. These numerical simulations show that recognizing AMSs in inferred images requires quite large areas covered by AMSs because of uneven illumination and limited spatial resolution. Also, higher-contrast structures with respect to the natural environment are obviously much more conspicuous and easier to infer than structures with an albedo similar to that of the environment.

Distinguishing such AMSs from high- and low-albedo natural environments (e.g., bright ice caps and mountain tops, dark lava fields and water reservoirs, etc.) may be a challenge unless they have a regular structure (like a power plant). Also, analyzing the spectral content of the reflected light can be

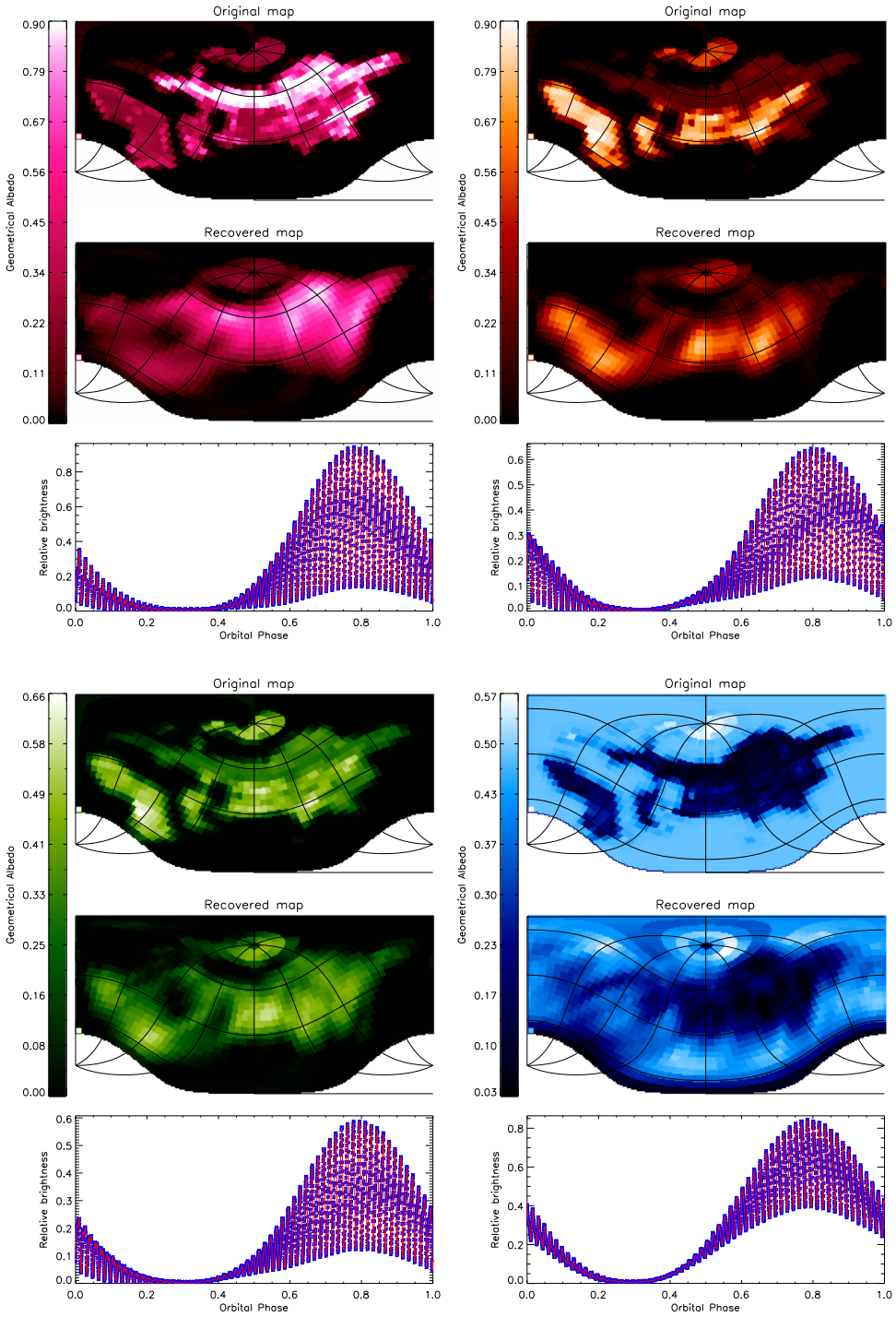

Figure 18. Same as Figure 5 but for the input maps in the four RGB+NIR bands from an exo-Earth image shown in the top panel of Figure 17. The RGB composite of the recovered images is shown in the bottom panel of Figure 17. The map quality indexes are IR: IQ = 82%, SD = 16%; R: IQ = 86%, SD = 15%; G: IQ = 88%, SD = 15%; B: IQ = 86%, SD = 25%.

useful. As mentioned above, the reflectance of AMSs can be limited to particular wavelengths. As examples, in Figure 22, we show the input and recovered spectra of the AMSs with absorbing and reflecting panels. The stationary nature of AMSs could also be an important factor in their identification.

6. Proxima b and the Alpha Centauri System

The Alpha Centauri system stars A and B and Proxima Centauri are the closest stars to the Sun. There is at least one exoplanet discovered so far in this system: Proxima b (Anglada-Escudé et al. 2016). Gas giant, Jupiter-like planets are concluded to be incompatible with the present measurements (Endl et al. 2015). Proxima b is an excellent candidate for first-time EPSI.

Proxima b orbits the M5 red dwarf within its WHZ with a period of about 11.2 days at about 0.04 au from the star. At this close distance, tidal interactions may have locked the axial rotation of the planet to its orbital period or to the 3:2 resonance as for Mercury. The presence of a dense atmosphere may influence the tidal interaction too (Kreidberg & Loeb 2016).

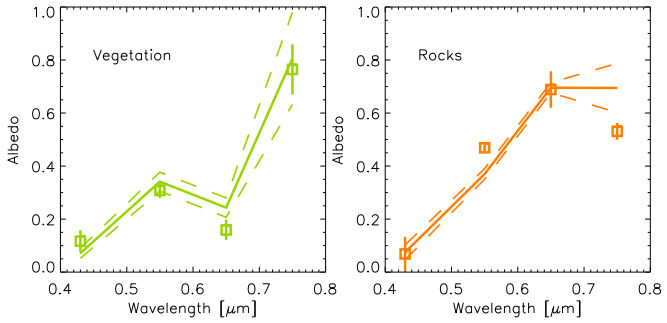

Figure 19. Average spectra of selected areas from the images in Figure 17. Left: spectra of a small green area at midlatitudes in the eastern part of the planet image. Right: spectra of a small desert area at lower latitudes in the western part of the planet image. Solid lines are the original image spectra. Dashed lines show a range of "natural" variations within the area in the original image. Symbols depict spectra from the recovered image. The presence of chlorophyll-rich organisms is unambiguously detected. The composition of the desert surface can be recovered by a comparison with spectra of minerals.

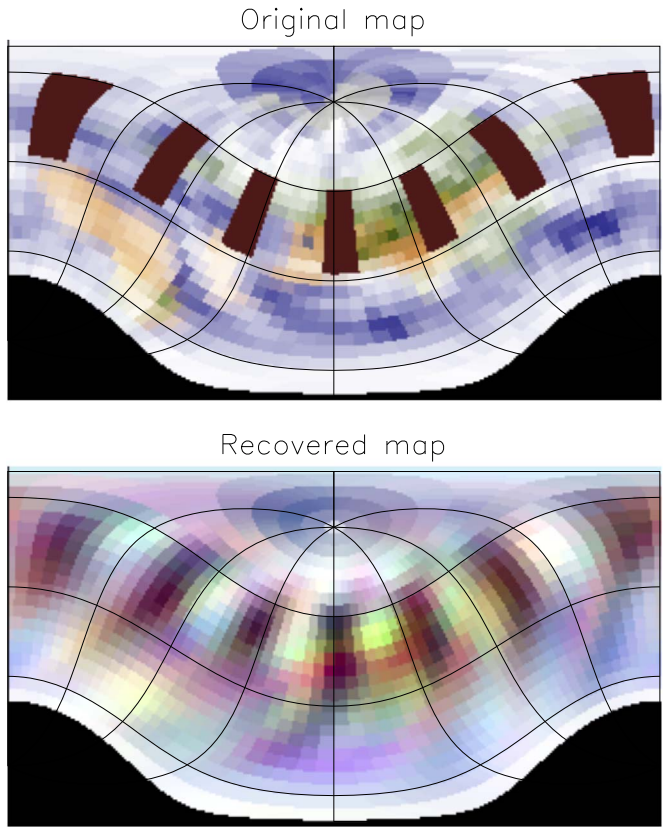

Figure 20. The RGB composite original and recovered maps of an exo-Earth with an AMS of low albedo (0.05) above clouds as a technosignature imitating a photovoltaic-like power plant in space.

In this section, we present simulations and inversions for the Proxima b planet assuming tidally locked orbits at the 1:1 and 2:3 resonances, with the planetary axis inclined with respect to the orbit plane.

Since Proxima b was discovered using the radial velocity (RV) technique, and so far no transits have been detected, the inclination of the orbit is still unknown. Thus, the planet could be an Earth-like planet of 1.3–1.5 M_E at i_o of 90°−60°, a super-Earth of 1.6–5 M_E at i_o of 55°−15°, or a Uranus/Neptune-mass planet of 15–17 M_E at $i_o \approx 5°$. Extremely low orbit inclinations

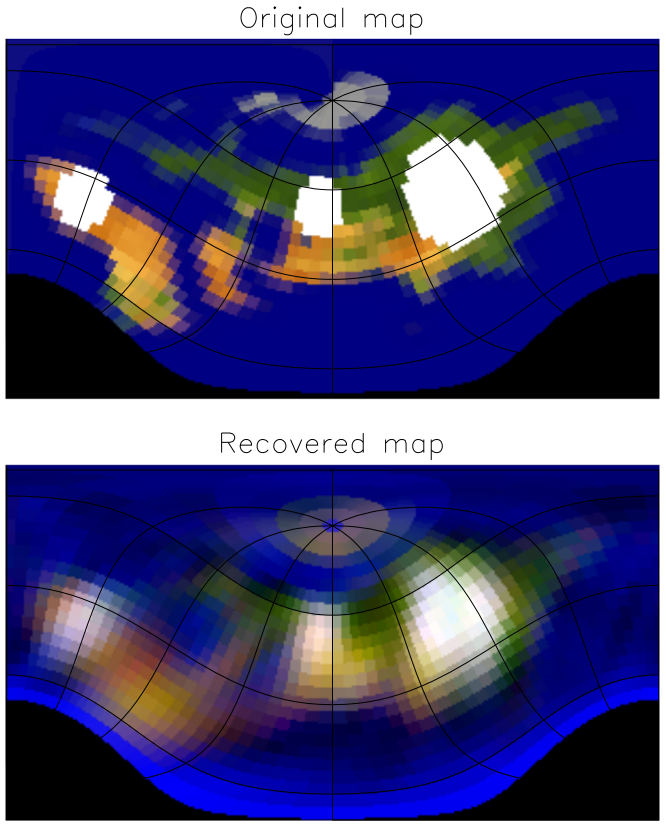

Figure 21. The RGB composite original and recovered maps of an exo-Earth with an AMS of high albedo (0.9) as a technosignature imitating urban-like areas under reflective "umbrellas" (white circles).

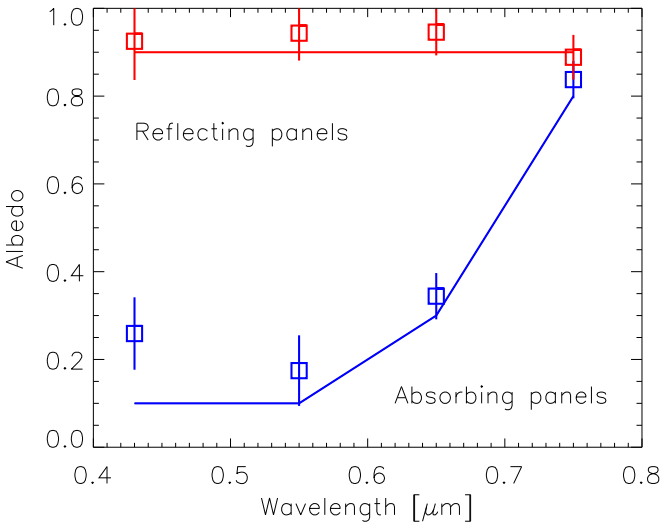

Figure 22. Average spectra of the AMSs shown in Figures 20 and 21. The solid lines and symbols show original and recovered spectra, respectively. Red and blue colors stand for spectra of the AMS panels with high and low albedo, respectively.

$i_o < 5°$ (a nearly face-on orbit) are still possible with a few percent chance, which may lead up to a Saturn-mass planet at $i_o \approx 1°$. The composition and, hence, the surface (or cloud) albedo of such planets may differ significantly. Therefore, obtaining albedo maps (especially at different wavelengths/passbands) can provide a powerful constraint on the planet mass and composition, as well as its potential habitability.

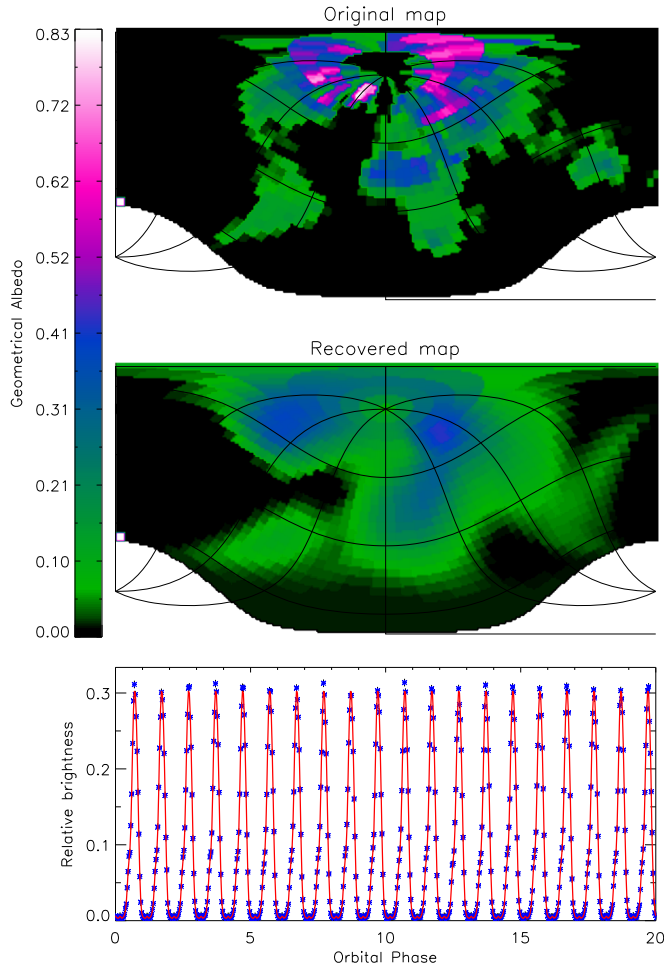

Figure 23. Same as Figure 5 but for the Proxima b model with S/N = 100 and the planet rotation being locked to the orbital motion at the 1:1 resonance. The light curve is simulated as it would be observed during several (20) orbital periods with 30 phase measurements per period, i.e., $N = 600$. Here IQ = 80% and SD = 13%.

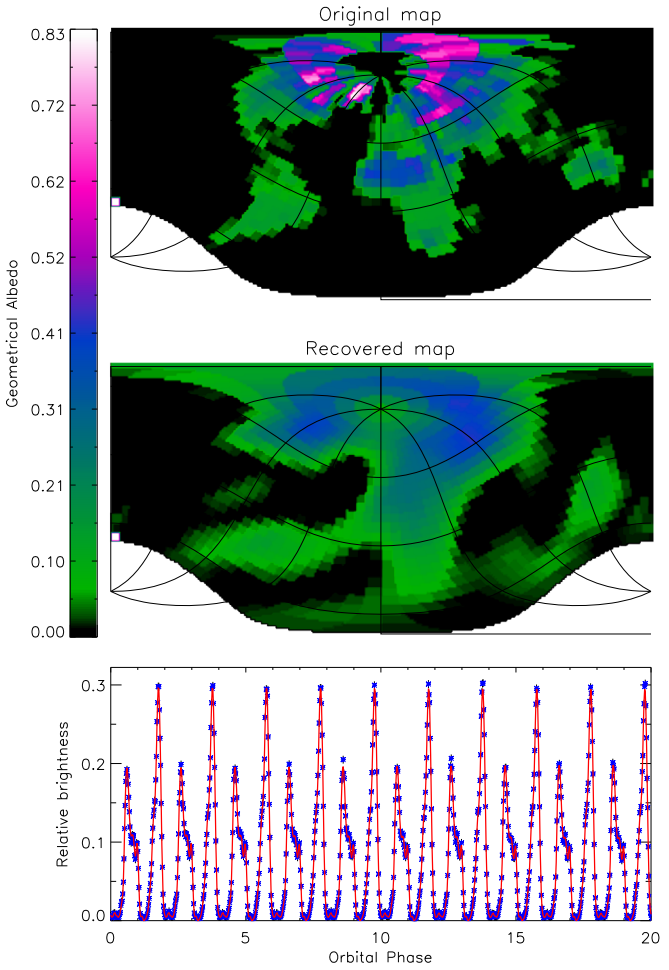

Figure 24. Same as Figure 23 but for the 3:2 resonance. Here IQ = 80% and SD = 13%.

As in Section 3.1, we test our inversion technique for Proxima b parameters using cloudless Earth's albedo maps. We assume an orbit inclination of 60° corresponding to a 1.5 M_E planet. With a terrestrial mean density of 5.5 g cm^{-3}, its radius would be 1.15 R_E, which we use in our reflected light simulations. Here an S/N = 100 is assumed.

The two scenarios when the planet rotation is locked to the orbital motion at the 1:1 and 3:2 resonances are shown in Figure 23 and 24, respectively. The fact that the periods are the same or very close hinders the amount of information in the light curve, even though we allow observations during several orbital periods. However, most of the landmass (80%) is still recovered, and its outline is quite recognizable. The quality of the map is higher for the 3:2 resonance orbit because there are two different light curves observed every other orbital period. Here the number of measurements and the S/N can be increased by observing during several orbital periods, as shown in our inversions.

Since the rotational axis inclination angle and the orbit normal azimuth are unknown, we vary them to understand the imaging capabilities of this planet, possibly locked at a resonance rotation. The IQ and SD parameters of our inversions for the periods locked at 1:1 are shown in Figure 25. Similar to the unlocked case, the most favorable planet axis inclination angles range within 30°–60°, while the orbit normal azimuth angle can be in a wide range.

7. Observational Requirements

In this section, we investigate and formulate observational requirements for the telescope size and scattered light level in order to obtain spectral images of Proxima b and possible rocky planets in the nearest-to-the-Sun stellar system Alpha Centauri A and B. We also estimate how many Earth-size and super-Earth planets in the WHZ can be imaged with our EPSI technique depending on the telescope aperture for a given scattered light background. To our knowledge, a large diffraction-limited coronagraphic telescope has not been built, so our noise estimates here do not reflect the real-world issues that we cannot readily model. These estimates are lower limits and should, at least, serve to motivate future efforts.

7.1. Contrast Profile

The level of the stellar scattered light, or contrast C with respect to the central star brightness, plays an important role in the planet reflected light S/N. The required S/N has to be achieved above the bright background at the WHZ angular distance from the star, where an Earth-like planet may reside. This component of the S/N budget is missing in the

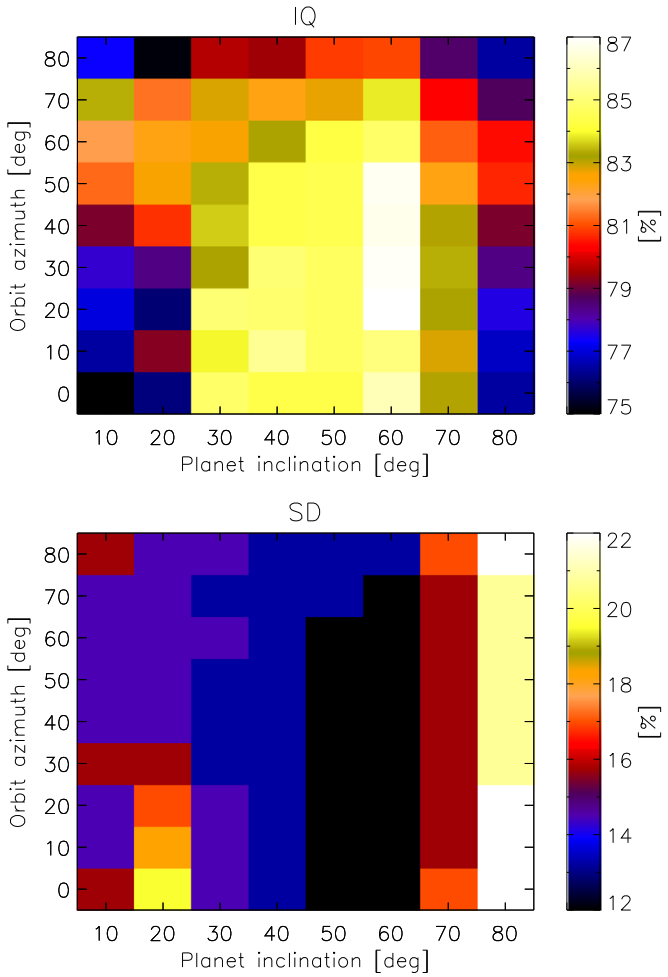

Figure 25. Dependence of the IQ parameter (Equation (6)) and map SD on the planet axis inclination angles i_r and the orbit normal azimuth ζ_o for the Proxima b model with the periods locked at 1:1. High values are in light tones, and low values are in dark tones. The median values of IQ and SD are 80% and 16%.

computations made by Fujii & Kawahara (2012) and leads to unrealistic sensitivities.

For reference, we take the contrast curve similar to the existing state-of-the-art performance achieved with the SPHERE imaging instrument at the Very Large Telescope (VLT; Langlois et al. 2014; M. Langlois 2017, private communication) using adaptive optics (AO) and spectral and angular differential imaging. We have also attempted to semi-quantitatively include the effects of wavefront phase errors, i.e., "speckle noise" (Aime & Soummer 2004), by scaling this coronagraph/AO-limited curve to other telescopes. A representative contrast profile that varies with the angle θ from the central star, expressed in units of the ratio of the wavelength λ to the diameter D, is shown in Figure 26.

We emphasize that this contrast curve is achieved for a telescope with an unsegmented primary mirror. For a highly segmented primary mirror without advanced segmented coronography and speckle-nulling AO, the contrast curve suffers from scattering off the segment edges and may not reach even 10^{-5} contrast at the required angular separation.

We expect that the contrast of Keck-style telescopes (with a multisegmented primary mirror and a single secondary mirror) will be worse than that of an unsegmented telescope by approximately a factor equal to the number of mirror segments

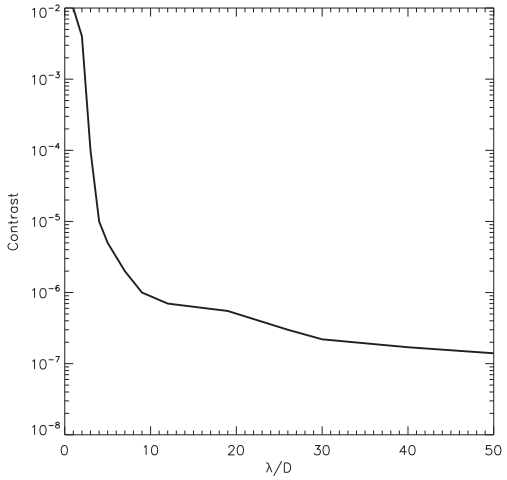

Figure 26. Assumed contrast curve for the scattered stellar light brightness vs. the angular distance from the star in units of the ratio of the wavelength λ to the telescope diameter D (for an unsegmented mirror telescope). The contrast reaches 10^{-7} at $\lambda/D = 100$.

in the full aperture. For example, we scale up the SPHERE C profile with factors of 50, 500, and 800 to obtain rough estimates of the S/N and number of detectable WHZ planets using Keck-, TMT-, and EELT-like telescopes with segmented primary mirrors.

On the other hand, recently proposed hybrid interferometric telescopes, such as the 74 m Colossus or 20–25 m ExoLife Finder (ELF), can achieve a contrast performance comparable to or even better than that of single-mirror telescopes (Kuhn et al. 2014; Moretto et al. 2014), at least in selected parts of their field of view (FOV). Such an optical system consists of an array of off-axis telescopes from a common parent parabola. Each off-axis telescope consists of the active primary and adaptive secondary mirrors. They build a common focus pupil image with an angular resolution equivalent to the diameter of the telescope array. Analogous to the nulling interferometry, independent off-axis apertures can be phased to "synthesize" a point-spread function (PSF) with a dark hole of extremely low scattered light and speckle noise. This dark hole can be moved within the FOV to follow an exoplanet orbiting the star by readjusting the aperture phases. Therefore, for simplicity, we assume here that the contrast curve shown in Figure 26 is also valid for a Colossus/ELF-type telescope at the location of an exoplanet.

Another improvement of the telescope/coronagraph performance can be achieved by using polarimetry to enhance the contrast of polarized light reflected from a planet above the stellar background. This technique has been employed for detection and detailed studies of circumstellar disks (e.g., Kuhn et al. 2001; Oppenheimer et al. 2008; Benisty et al. 2015; Follette et al. 2017), as well as exoplanets unresolved from their stars (Berdyugina et al. 2008, 2011). The direct imaging instruments SPHERE at the VLT and GPI at Gemini have this option and are successful in imaging circumstellar disks and resolved companions.

An important contribution to the S/N budget for ground-based telescopes is the brightness of the sky. We have used sky magnitudes for the dark time at the ESO Paranal Observatory, Chile, by Patat (2008), while averaging variations due to the 11 yr solar cycle. We note that the sky contribution is more

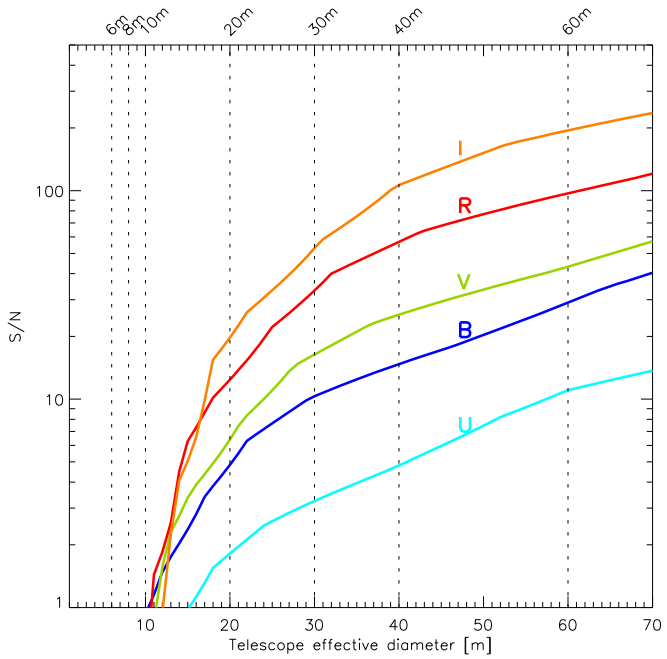

Figure 27. The S/N curves for an Earth-like planet like Proxima b (see parameters in the text), depending on the effective telescope diameter, when assuming a single, unsegmented primary mirror. The S/N is computed for a 1 hr exposure time in the *UBVRI* passbands, when only half of the planet is illuminated. The assumed contrast curve for the stellar scattered light is shown in Figure 26. The planet average surface albedo in all bands is assumed to be 0.2 for simplicity, which allows one to scale the S/N for other albedo values. Vertical dashed lines indicate the effective diameters (unsegmented) of the existing and planned telescopes. The resolving power of the telescopes is assumed to be defined by the effective diameter.

important for fainter stars observed with smaller telescopes. As the aperture of the telescope increases, the size of the resolution element decreases, and the sky contribution decreases as well.

Thus, we compute the number of photons from three different sources: the planet itself, the scattered stellar background at a given angular separation from the star, and a sky background area equal to the resolution element of a given telescope aperture. In this way, in the following sections, we compute the S/N for exoplanets in the standard Johnson *UBVRI* bands, depending on the size of the telescope, using known stellar and planetary parameters.

7.2. S/N for Proxima b

Achieving S/N = 100 in the reflected light from an exoplanet is rather challenging even for the nearest exoplanet, such as Proxima b. Here we compute the S/N in the *UBVRI* passbands for a 1 hr exposure time when assuming a telescope efficiency of 25%, an illumination phase of the planet of 0.5 (maximum elongation from the star), and an average surface albedo in all bands of 0.2. The stellar magnitudes used are from the SIMBAD database. The result is shown in Figure 27.

Such an S/N computation produces photon-limited estimates that can be considered as some realistic upper-limit values. Systematic errors are usually specific to a particular instrument design and calibration and data reduction procedures. Hence, we assume here the best-case scenario, when all other errors are reduced down to the photon noise level. In practice, to detect reflected light variability, one should also allow for smaller illumination phases (down to at least 0.1) and surface albedo (down to 0.05). For example, the reflectance of vegetation in the optical is about 0.05. The reflectance of rocky terrain and deserts is between 0.1 and 0.15, and that of the ocean is 0.1 in the blue (due to sky reflection) and less than 2% in the red and NIR. The glint on the ocean due to Fresnel sunlight reflection is very bright, but its relative contribution with respect to landmasses is low.

We also note that because of the orbit inclination to the line of sight, the star–planet projected angular separation varies with the orbital phase, leading to different C levels at different orbital phases. Hence, orbital phases near conjunctions will be hindered by higher C and, therefore, lower S/N for the same exposure time. For example, for the assumed orbit inclination of 60° for Proxima b, the angular separation between the star and the planet varies by a factor of 2, i.e., between 37 mas at maximum elongations and 18 mas near conjunctions. Thus, observing Proxima b near conjunction phases may require a telescope system with a larger resolving power or a better contrast at smaller θ angles, depending on the orbit inclination.

The overall conclusion from this exercise is that a telescope with low scattered light, an effective diameter $D \geqslant 12$ m, and an equivalent or larger angular resolving power is required for detecting an Earth-like Proxima b above the star and sky background in the *BVRI* bands with S/N $\geqslant 2$ during a 1 hr exposure time. A large telescope ($\geqslant$20 m) is preferable for more efficient observations.

The *BVRI* band measurements are particularly interesting for detecting possible photosynthetic life signatures, as described in Section 5.1 and Berdyugina et al. (2016). A 20 m class telescope should be able to achieve an S/N of 5–20 in the *BVRI* bands in 1 hr, at least near maximum elongations of the planet. The *R*-band measurements during several orbital periods with S/N = 20 will already be usable for surface inversions. With such a dedicated telescope in Chile, Proxima b can be observed between 3 and 7 hr night^{-1} for 6 months (February to July). Even when discarding 10% of the observing time for bad weather conditions, one can obtain about 800 1 hr measurements spread over 16 orbital periods within just one season. Observing in at least three adjacent passbands simultaneously (e.g., *BVR* or *VRI*) should be possible for the successful operation of the AO system.

Hence, after only one season of observations, we will be able to obtain the first "color photographs" of Proxima b. If the planet is partially cloudy, several observing seasons are needed to filter out the cloud noise and obtain more detailed surface maps. If planet is completely covered by thick clouds or its surface is completely featureless, we will be able to conclude on its bulk properties already after a few orbital periods (1–2 months). If an atmosphere is present on Proxima b (e.g., Lovis et al. 2017), it can also be detected and studied for life signatures with the ELF-type telescope (Berdyugina et al. 2018b).

7.3. S/N for Alpha Centauri A and B Potential Planets

A search for planets around the Alpha Centauri A and B components has already ruled out Jupiter-like planets in their WHZ (Endl et al. 2015), but there is still hope for smaller planets, which were not yet detected or ruled out due to sensitivity limits. If any planets in the WHZ of these stars are found, they will be excellent targets for our indirect surface imaging.

We have computed the S/N diagram for an Earth-size planet with an average geometrical albedo of 0.2 and at the half-

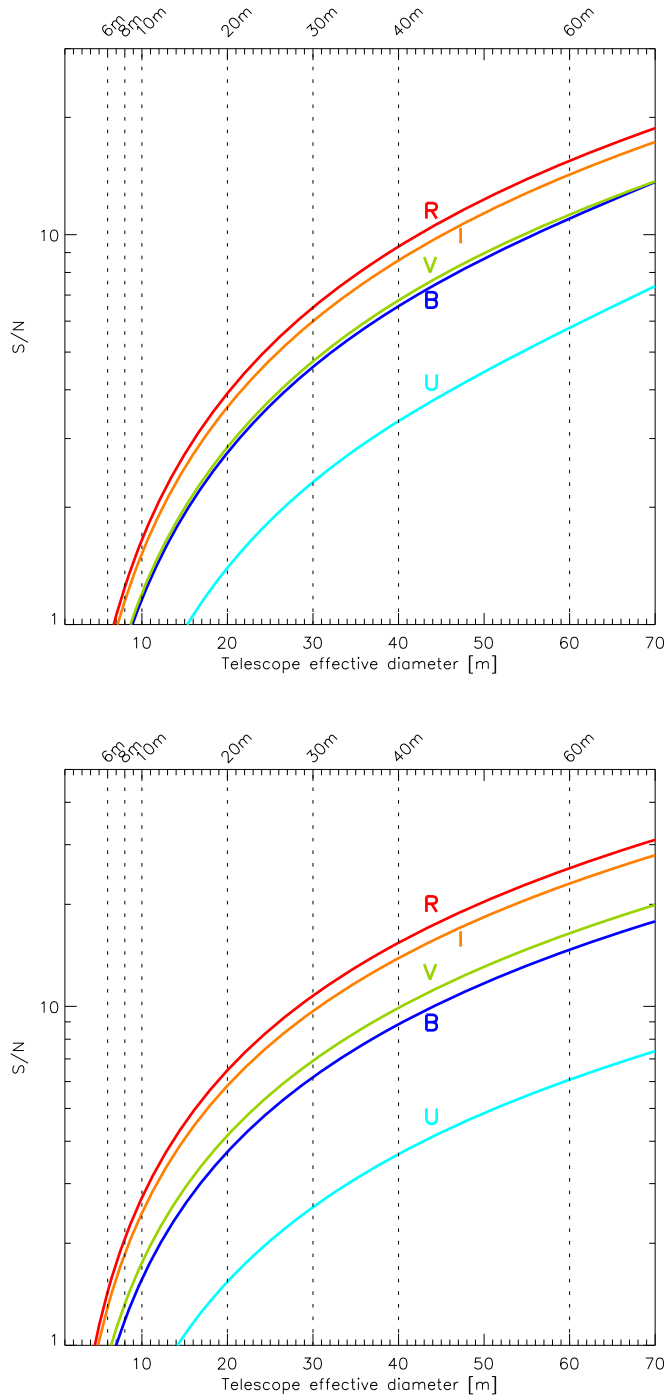

Figure 28. Same as Figure 27 but for α Cen A and B (top and bottom) hypothetical Earth-size planets residing in their corresponding WHZs.

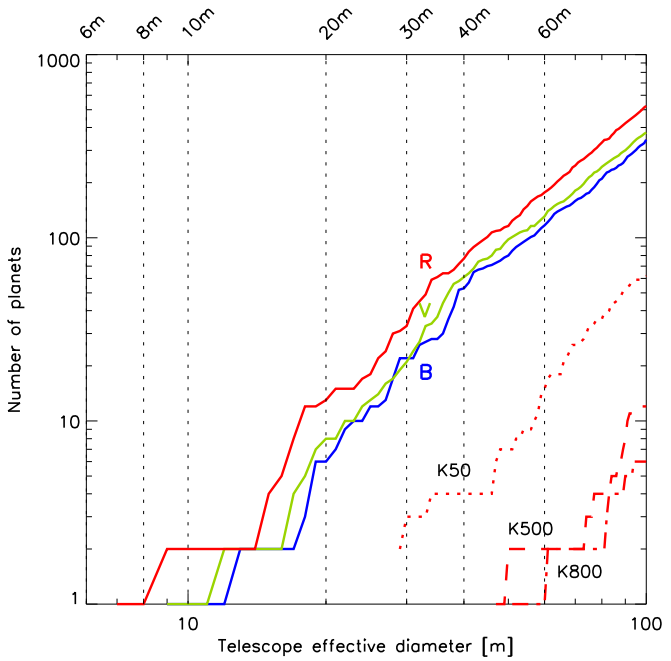

Figure 29. Number of detectable WHZ Earth-size planets (1 R_E) in the *BVR* bands (S/N $\geqslant$ 5) around AFGKM main-sequence stars brighter than $V = 13$ mag. Solid lines are for unsegmented or interferometric telescopes, which can achieve the contrast shown in Figure 26. Dotted, dashed, and dashed–dotted lines are for Keck-type telescopes (segmented primary and single secondary mirrors) with 50, 500, and 800 segments, respectively. Here the exposure time is 4 hr, the planet albedo is 0.2 in all bands, and the illumination phase is 0.5.

illumination orbital phase within the WHZ of the Alpha Centauri A and B stars—about 930 and 560 mas, respectively (see Figure 28). Resolving the WHZ of these stars is theoretically possible even with a 1 m class telescope, but achieving a significantly higher contrast level is needed for detecting Earth-size planets around these more luminous stars. Hence, such planets may remain undetectable in the optical or NIR with 8–10 m class telescopes, but they can be easily detected with a 20 m class telescope, assuming the contrast curve shown in Figure 26.

Our result suggests that formally, with a longer exposure time ($\geqslant$10 hr), an Earth-like WHZ planet may be detected around Alpha Cen B with an 8 m telescope at S/N = 5. In practice, however, systematic errors accumulated over several nights may prevent achieving the photon-limited S/N. Also, if the planetary orbit is coplanar with the binary (AB) orbit, i.e., $i_o \approx 80°$, such a detection is only possible at planet maximum elongations from the star. Near the "full-moon" phase, the planet–star angular separation is reduced by a factor of almost 6, which leads to a severe increase of the stellar light background and makes such a planet undetectable. Considering that the orbit orientation on the sky plane is also unknown, the direct detection of an Earth-size planet in the WHZ of Alpha Cen B with an 8 m telescope may take a long time.

Similar to the Proxima b case discussed in the previous section, dedicated continuous direct imaging observations of the Alpha Centauri A and B stars with a larger telescope may reveal (or exclude) Earth-size planets in their WHZ. Obviously, larger planets can be detected within a shorter observing time, as the S/N increases with the size of the planet. The advantage here is that these planets will most likely have axial rotation periods different from the orbital periods (not tidally locked), which will allow for a more detailed surface mapping, as presented in Section 3.

7.4. Number of Detectable Exoplanets

Assuming the telescope and instrument performance as in Section 7.2, we can evaluate how many WHZ Earth-size planets in the solar neighborhood can be potentially detected and surface-imaged. From the SIMBAD database, we have compiled a list of several thousand AFGKM main-sequence stars brighter than $V = 13$ mag. We have computed their WHZ distances by scaling the Sun–Earth WHZ with the stellar luminosity for an Earth-like planet. The reflected light flux is

Table 2
Dwarf Stars in the Solar Neighborhood Where WHZ Earth-size Planets Can Be Potentially Detected and Mapped

Star Name	Star Number	$d(^*)$ (lt-yr)	Sp.	B (mag)	V (mag)	R (mag)	d(WHZ) (mas)	S/N (B)	S/N (V)	S/N (R)	α_{2000} (h:m:s)	δ_{2000} (deg:arcmin: arcsec)	Exoplanets
Proxima Cen	GJ 551	4.24	M5	12.95	11.13	9.45	31.7	14.4	19.6	35.7	14:29:43	−62:40:46	b (1)
Barnard's	GJ 699	5.96	M4	11.24	9.51	8.30	40.7	11.8	18.0	27.3	17:57:48	4:41:36	b (2)
Ross 128	GJ 447	11.00	M4	12.90	11.15	9.86	22.1	⋯	⋯	5.7	11:47:44	0:48:16	b (3)
LHS 33	GJ 273	12.40	M3	11.44	9.87	8.70	32.2	⋯	⋯	5.8	7:27:25	5:13:33	b, c (4)
LHS 58	GJ 725A	11.49	M3	10.45	8.91	8.10	34.3	5.6	6.7	8.5	18:42:47	59:37:49	
Ross 154	GJ 729	9.70	M3	12.23	10.49	9.28	41.2	⋯	⋯	6.5	18:49:49	−23:50:10	
LHS 450	GJ 687	14.84	M3	10.65	9.15	8.30	27.0	⋯	⋯	5.9	17:36:26	68:20:21	
CD-4611540	GJ 674	14.84	M3	10.97	9.41	8.34	27.0	⋯	⋯	5.7	17:28:40	−46:53:43	b (5)
LHS 59	GJ 725B	11.49	M3	11.28	9.69	8.90	35.5	⋯	⋯	6.3	18:42:47	59:37:36	
LHS 37	GJ 411	8.31	M2	8.96	7.52	6.60	59.5	9.1	13.2	20.9	11:3:20	35:58:12	? (6)
GX And	GJ 15A	11.62	M2	9.63	8.13	7.30	42.3	6.1	8.4	10.9	0:18:23	44:1:23	b (7)
LHS 38	GJ 412A	15.81	M2	10.27	8.78	7.90	31.3	⋯	⋯	5.3	11:5:29	43:31:36	
LHS 70	GJ 887	10.72	M2	8.82	7.34	6.39	46.3	9.2	12.6	19.2	23:5:52	−35:51:11	
LHS 30	GJ 205	18.60	M1	9.44	7.97	7.00	33.1	⋯	⋯	5.7	5:31:27	−3:40:38	
LHS 386	GJ 570B	19.32	M1	9.56	8.06	7.07	31.6	⋯	⋯	5.2	14:57:27	−21:24:42	
LHS 1827	GJ 229A	18.78	M1	9.61	8.13	7.16	32.5	⋯	⋯	5.1	6:10:35	−21:51:53	b (8)
LHS 260	GJ 338A	20.66	M0	9.07	7.63	6.80	46.2	⋯	⋯	5.0	9:14:23	52:41:12	
AX Mic	GJ 825	12.95	M0	8.09	6.68	5.83	68.0	⋯	6.4	10.1	21:17:15	−38:52:3	
LHS 280	GJ 380	15.88	K8	7.98	6.61	5.80	62.1	⋯	5.1	7.8	10:11:22	49:27:15	
61 Cyg B	GJ 820B	11.40	K7	7.40	6.03	4.86	95.0	5.6	6.5	11.3	21:6:55	38:44:31	
HR 486	GJ 66B	26.72	K5	6.84	5.96	5.32	59.2	⋯	⋯	5.4	1:39:48	−56:11:36	
Eps Ind	GJ 845A	11.87	K5	5.75	4.69	4.05	110.4	9.6	9.6	12.3	22:3:22	−56:47:10	
61 Cyg A	GJ 820A	11.41	K5	6.39	5.21	4.19	114.7	7.3	7.9	11.9	21:6:54	38:44:58	
KX Lib	GJ 570A	19.19	K4	6.85	5.74	5.13	75.1	⋯	⋯	5.4	14:57:28	−21:24:56	? (9)
36 Oph A	GJ 663A	19.44	K2	5.93	5.08	4.52	88.4	⋯	⋯	5.3	17:15:21	−26:36:06	
36 Oph B	GJ 663B	19.44	K1	5.88	5.03	4.49	96.9	⋯	⋯	<5.0	17:15:21	−26:36:10	
Eps Eri	GJ 144	10.49	K2	4.61	3.73	3.17	163.9	11.1	11.9	15.9	3:32:56	−9:27:30	b (10)
70 Oph A	GJ 702A	16.58	K0	4.97	4.13	3.60	124.4	5.7	5.5	6.7	18:5:27	2:29:59	
40 Eri	GJ 166A	16.42	K0	5.23	4.41	3.89	126.9	5.2	5.1	6.0	4:15:16	−7:39:10	HD 26965b (11)
Alpha Cen B	GJ 559B	4.32	K1	2.21	1.33	0.50	533.7	22.2	26.2	42.2	14:39:35	−60:50:15	
Tau Cet	GJ 71	11.75	G8	4.22	3.50	3.03	201.1	7.3	7.5	9.6	1:44:4	−15:56:15	efgh (12)
Alpha Cen A	GJ 559A	4.32	G2	0.72	0.01	−0.55	930.3	14.7	16.0	22.7	14:39:36	−60:50:2	

Note. A 25 m telescope with a high-contrast performance can detect Earth-size (1 R_E) exoplanets within the WHZ of these stars with S/N $\geqslant$ 5 in at least one of the *BVR* passbands. Exoplanets are assumed to have an average geometrical albedo of 0.2 in all passbands, and the illumination phase is 0.5. The exposure time is 8 hr. The distance to the star $d(^*)$ from the Sun is in light-years (lt-yr). The WHZ distance from the host star d(WHZ) is in milliarcseconds. References for exoplanets: (1) Anglada-Escudé et al. (2016), (2) Ribas et al. (2018), (3) Dittmann et al. (2017), (4) Astudillo-Defru et al. (2017), (5) Bonfils et al. (2007), (6) Butler et al. (2017), (7) Howard et al. (2014), (8) Tuomi et al. (2014), (9) Endl et al. (2000), (10) Hatzes et al. (2000), (11) Ma et al. (2018), (12) Feng et al. (2017).

computed using the Earth's size, geometrical albedo of 0.2 for all passbands, and 0.5 illumination phase. We consider a planet detectable if S/N $\geqslant$ 5 can be achieved during 4 hr exposure time.

The number of Earth-size (1 R_E) detectable planets is plotted for different telescope sizes and types in Figure 29. The plot shows that a 25 m class telescope with a SPHERE-like performance (like the ELF) can detect and surface-image dozens of WHZ Earth-size planets, depending on the exposure time. A sample of nearby stars where such planets can be detected with such a 25 m telescope with S/N $\geqslant$ 5 during an 8 hr exposure time is presented in Table 2. Several (generally, larger than Earth) exoplanets have already been confirmed around those stars. These stars and planets are the first targets for the ELF telescope. Hundreds of Earth-size planets in this magnitude-limited sample could be detected by a 70 m telescope (like the Colossus). However, we evaluate that most likely none of Earth-size planets can be detected by Keck-style telescopes with $D < 45$ m.

The number of detectable Neptune-size exoplanets (4 R_E) is plotted for different telescope sizes and types in Figure 30. In this case, a 25 m coronagraphic telescope can detect and image hundreds of planets, while all such planets can be discovered and imaged with a 60 m high-performance telescope. Multi-segmented Keck-style telescopes, such as TMT and EELT, should be able to collect enough photons above the stellar background for tens of such planets. Jupiter-size planets are more realistic targets for such telescopes.

8. Summary and Conclusions

This paper demonstrates that for many exoplanets, it should be possible to map their surface or cloud structures using reflected starlight analyzed with the EPSI technique. Given the results presented in this paper, we find that there is enough information in the light curve to perform 2D reconstructions of exoplanet surface features. We have shown that time-resolved exoplanet photometry with an S/N as low as 20 can yield, for example,

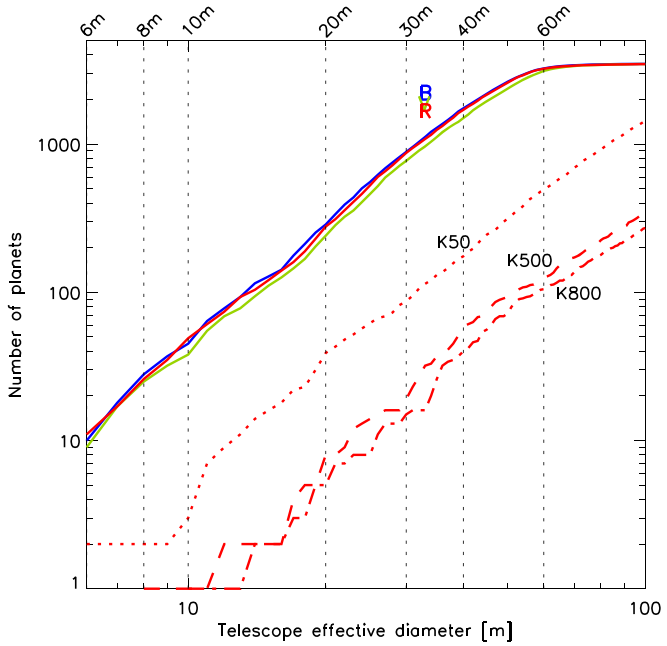

Figure 30. Same as Figure 29 but for planets of 4 R_E, which is about the size of Neptune. All such planets (and bigger ones) in the solar neighborhood could be detected and surface-imaged with a 70 m Colossus-like telescope.

detection of continents on a water-rich world. With higher S/N, it may be possible to trace the outline of continents and their large-scale albedo features, such as deserts, vegetation areas, snow-fields, ice caps, etc., or even artificial (mega-)structures.

Combining EPSI with spectrally resolved data may yield information about exoplanetary subcontinental-scale biomarkers. Planetary "noise" like clouds would limit such observations, but under some circumstances only by decreasing the surface albedo contrast.

These data are within reach of the next generation of coronagraphic telescopes. For example, a dedicated hybrid telescope interferometer of 12–20 m diameter could generate surface maps in different colors for the nearest exoplanet, Proxima b, and a few others. Dozens of Earth-size exoplanets and hundreds of larger planets could be imaged this way with a hybrid telescope of 25 m or larger diameter.

S.V.B. acknowledges support by the ERC Advanced Grant HotMol (www.hotmol.eu). J.R.K. acknowledges support by the Alexander von Humboldt Foundation, Germany. We are very thankful to Dr. Henrik Hargitai for valuable comments on the manuscript.

References

Adhikari, R., Beichman, C., Berea, A., et al. 2018, arXiv:1812.08681
Aime, C., & Soummer, R. 2004, ApJL, 612, L85
Amundsen, D. S., Mayne, N. J., Baraffe, I., et al. 2016, A&A, 595, A36
Angerhausen, D., Enriquez, E., Howard, A., et al. 2018, arXiv:1812.08681
Anglada-Escudé, G., Amado, P. J., Barnes, J., et al. 2016, Natur, 536, 437
Astudillo-Defru, N., Forveille, T., Bonfils, X., et al. 2017, A&A, 602, A88
Benisty, M., Juhasz, A., Boccaletti, A., et al. 2015, A&A, 578, L6
Berdyugina, S. V. 1998, A&A, 338, 97
Berdyugina, S. V. 2017, arXiv:1607.06874
Berdyugina, S. V., Batalha, N., Adhikari, R., et al. 2018a, arXiv:1812.08681
Berdyugina, S. V., Berdyugin, A. V., Fluri, D. M., & Piirola, V. 2008, ApJL, 673, L83
Berdyugina, S. V., Berdyugin, A. V., Fluri, D. M., & Piirola, V. 2011, ApJL, 728, L6
Berdyugina, S. V., Berdyugin, A. V., Ilyin, I., & Tuominen, I. 1998, A&A, 340, 437
Berdyugina, S. V., Kuhn, J. R., Harrington, D. M., Santl-Temkiv, T., & Messersmith, E. J. 2016, IJAsB, 15, 45
Berdyugina, S. V., Kuhn, J. R., Langlois, M., et al. 2018b, Proc. SPIE, 10700, 107004I
Berdyugina, S. V., Pelt, J., & Tuominen, I. 2002, A&A, 394, 505
Bonfils, X., Mayor, M., Delfosse, X., et al. 2007, A&A, 474, 293
Bréon, F. M., Buriez, J. C., Couvert, P., et al. 2002, AdSpR, 30, 2383
Buie, M. W., Young, E. F., & Binzel, R. P. 1997, in Pluto and Charon, ed. S. A. Stern & D. J. Tholen (Tucson: Univ. Arizona Press), 269
Butler, R. P., Vogt, S. S., Laughlin, G., et al. 2017, AJ, 153, 208
Carbognani, A., Tanga, P., Cellino, A., et al. 2012, P&SS, 73, 80
Catling, D. C., Krissansen-Totton, J., Kiang, N. Y., et al. 2018, AsBio, 18, 709
Coffeen, D. L. 1979, JOSA, 69, 1051
Cowan, N. B., & Agol, E. 2008, ApJL, 678, L129
Cowan, N. B., Agol, E., Meadows, V. S., et al. 2009, ApJ, 700, 915
Cowan, N. B., Chayes, V., Bouffard, E., Meynig, M., & Haggard, H. M. 2017, MNRAS, 467, 747
Cowan, N. B., Fuentes, P. A., & Haggard, H. M. 2013, MNRAS, 434, 2465
Cowan, N. B., & Fujii, Y. 2017, in Handbook of Exoplanets, ed. H. J. Deeg & J. A. Belmonte (Cham: Springer), 147
Crossfield, I. J. M., Hansen, B. M. S., Harrington, J., et al. 2010, ApJ, 723, 1436
de Wit, J., Gillon, M., Demory, B.-O., & Seager, S. 2012, A&A, 548, A128
Demory, B.-O., Seager, S., Madhusudhan, N., et al. 2011, ApJL, 735, L12
Dittmann, J. A., Irwin, J. M., Charbonneau, D., et al. 2017, Natur, 544, 333
Dyudina, U., Zhang, X., Li, L., et al. 2016, ApJ, 822, 76
Endl, M., Bergmann, Ch., Hearnshaw, J., et al. 2015, IJAsB, 14, 305
Endl, M., Krster, M., & Els, S. 2000, A&A, 362, 585
Evans, T. M., Pont, F., Sing, D. K., et al. 2013, ApJL, 772, L16
Faigler, S., & Mazeh, T. 2015, ApJ, 800, 73
Feng, F., Tuomi, M., Jones, H. R. A., et al. 2017, AJ, 154, 135
Fluri, D. M., & Berdyugina, S. V. 2010, A&A, 512, A59
Follette, K. B., Rameau, J., Dong, R., et al. 2017, AJ, 153, 264
Ford, E. B., Seager, S., & Turner, E. L. 2001, Natur, 412, 885
Fujii, Y., & Kawahara, H. 2012, ApJ, 755, 101
Grenfell, J. L. 2017, PhR, 713, 1
Guthnick, P. 1906, AN, 171, 273
Hansen, J. E., & Travis, L. D. 1974, SSRv, 16, 527
Harrington, J., Hansen, B. M., Luszcz, S. H., et al. 2006, Sci, 314, 623
Hatzes, A., Cochran, W. D., McArthur, B., et al. 2000, ApJL, 544, L145
Heng, K., & Showman, A. P. 2015, AREPS, 43, 509
Howard, A. W., Marcy, G. W., Fischer, D. A., et al. 2014, ApJ, 794, 51
Kaasalainen, M., Lamberg, L., Lumme, K., & Bowell, E. 1992, A&A, 259, 318
Karkoschka, E. 1994, Icar, 111, 174
Kawahara, H., & Fujii, Y. 2011, ApJL, 739, L62
Kiang, N. Y., Domagal-Goldman, S., Parenteau, M. N., et al. 2018, AsBio, 18, 619
Knutson, H. A., Charbonneau, D., Allen, L. E., et al. 2007, Natur, 447, 183
Komacek, T. D., & Showman, A. P. 2016, ApJ, 821, 16
Kreidberg, L., & Loeb, A. 2016, ApJL, 832, L12
Kuhn, J. R., & Berdyugina, S. V. 2015, IJAsB, 14, 401
Kuhn, J. R., Berdyugina, S. V., Langlois, M., et al. 2014, Proc. SPIE, 9145, 91451G
Kuhn, J. R., Potter, D., & Parise, B. 2001, ApJL, 553, L189
Langlois, M., Vigan, A., Dohlen, K., et al. 2014, Proc. SPIE, 9147, 91479P
Lovis, C., Snellen, I., Mouillet, D., et al. 2017, A&A, 599, A16
Ma, B., Ge, J., Muterspaugh, M., et al. 2018, MNRAS, 480, 2411
Majeau, C., Agol, E., & Cowan, N. B. 2012, ApJL, 757, L32
McClatchey, R., Fenn, R., Selby, J., Volz, F., & Garing, J. 1972, Optical Properties of the Atmosphere, U.S. Air Force Cambridge Research Labs AFCRL-72.0497
Meadows, V. S., Reinhard, C. T., Arney, G. N., et al. 2018, AsBio, 18, 630
Moretto, G., Kuhn, J. R., Thiebaut, E., et al. 2014, Proc. SPIE, 9145, 91451L
Morrison, D., Jones, T. J., Cruikshank, D. P., & Murphy, R. E. 1975, Icar, 24, 157
Oppenheimer, B. R., Brenner, D., Hinkley, S., et al. 2008, ApJ, 679, 1574
Patat, F. 2008, A&A, 481, 575
Rauscher, E., Menou, K., Seager, S., et al. 2007, ApJ, 664, 1199
Ribas, I., Tuomi, M., Reiners, A., et al. 2018, Natur, 563, 365
Russell, H. N. 1906, ApJ, 24, 1
Sagan, C., & Khare, B. 1979, Natur, 277, 102

Schwartz, J. C., Sekowski, C., Haggard, H. M., Palle, E., & Cowan, N. B. 2016, MNRAS, 457, 926
Schwieterman, E. W., Kiang, N. Y., Parenteau, M. N., et al. 2018, AsBio, 18, 663
Simon, A. A., Wong, M. H., & Orton, G. S. 2015, ApJ, 812, 55
Snellen, I. A. G., de Mooij, E. J. W., & Albrecht, S. 2009, Natur, 459, 543
Sobolev, V. V. 1956, Radiative Transfer in Stellar and Planetary Atmospheres (Gos. izd-vo tek.-teor. lit.: Moscow)
Tarter, J. C., Agrawal, A., Ackermann, R., et al. 2010, Proc. SPIE, 7819, 781902
Tuomi, M., Jones, H. R. A., Barnes, J. R., Anglada-Escude, G., & Jenkins, J. S. 2014, MNRAS, 441, 1545